POLITECNICO DI TORINO
Repository ISTITUZIONALE

Bending, free vibration and buckling of functionally graded carbon nanotube-reinforced sandwich plates, using the extended Refined Zigzag Theory

Availability:
This version is available at: 11583/2749014 since: 2019-08-29T19:37:00Z

Publisher:
Elsevier

Published
DOI:10.1016/j.compstruct.2019.111324

Terms of use:
openAccess

This article is made available under terms and conditions as specified in the corresponding bibliographic description in the repository

(Article begins on next page)

09 November 2022

Bending, free vibration and buckling of functionally graded carbon nanotube-reinforced sandwich plates, using the extended Refined Zigzag Theory

M. Di Sciuva and M. Sorrenti[1]

Department of Mechanical and Aerospace Engineering – Politecnico di Torino

Corso Duca degli Abruzzi, 24 10129 Torino, Italy

e-mails: marco.disciuva@polito.it, matteo.sorrenti@polito.it

Abstract.

The paper presents an application of the extended Refined Zigzag Theory (eRZT) in conjunction with the Ritz method to the analysis of bending, free vibration and buckling of functionally graded carbon nanotube-reinforced (FG-CNTR) sandwich plates. Two stacking sequences are taken into consideration: sandwich panels with a homogeneous core and functionally graded face-sheets and sandwich panels with homogeneous face-sheets and a functionally graded core.

After validating the convergence characteristics and the numerical accuracy of the developed approach using orthogonal and non-orthogonal admissible functions, a detailed parametric numerical investigation is carried out. Bending under bi-sinusoidal and uniform transverse pressure, free vibration and buckling loads under uniform in-plane uniaxial, biaxial and shearing loadings of FG-CNTR sandwich plates are studied. Numerical results for square and rectangular FG-CNTR sandwich plates under various combinations of geometry (core-to-face sheet thickness ratio and side to thickness ratio), different set of boundary conditions, CNTs volume fraction and grading laws are presented and discussed in detail. It is concluded that the eRZT predicts the response for static, stability and free vibration problems more accurately than first-order (FSDT) and third-order (TSDT) shear deformation theories, also for FG-CNTR sandwich plates.

***Keywords*:** Carbon nanotube-reinforced sandwich plates; functionally graded materials; extended Refined Zigzag Theory; bending; vibration; buckling; Ritz method.

---

[1] Corresponding Author: Matteo Sorrenti, email: matteo.sorrenti@polito.it Tel. +39 3337120343

1. Introduction

Due to their excellent characteristics such as low weight, high specific flexural stiffness, good fatigue, thermal and damping properties, high noise absorption, sandwich structures have been used in the last decades in transportation, aerospace, military, marine and civil structures applications [1]. Typically, sandwich structures consist of two thin stiff face-sheets and one core adhesively bonded between them. Core is typically made of metal honeycomb or foam materials. For face-sheets aluminium, steel, fiber-reinforced-polymers (FRPs) are usually used. FRPs are formed by fiber with an imposed orientation. The result is a laminate with different mechanical and thermal properties through the thickness. The main problems affecting this kind of sandwich structures are stresses concentration between layers (delamination) due to the different material properties, matrix cracks, imperfect bonding of the layers or between face-sheets and core [2,3]. To avoid these damages, during the 1980s, in Japan there has been developed a new class of materials, the Functionally Graded Materials [4]. These materials are formed by varying, with a specific grading law, the mechanical and thermal properties between two or more phases mixed together. During the last decades, their applications were extended in different areas, such as aerospace and civil structures, military applications, medical fields, energy and sensors [5–14].

Experimental investigations showed that carbon nanotubes (CNTs) have extraordinary mechanical properties over continuous carbon fibers [15,16]. Moreover, the addition of small volume fraction of single-walled carbon nanotubes (SWCNT) or double-walled carbon nanotubes (DWCNT) improve the mechanical characteristics (tensile modulus, yield strength and ultimate strengths) of the polymer films, and polymeric films with aligned CNTs as reinforcements exhibit superior strength compared to randomly oriented nanotubes, [17–21]. The aforementioned exceptional characteristics of CNTs make them a great candidate for reinforcing different polymer-based nanocomposites. Thus, in recent years, the concept of FG composite structures reinforced with SWCNT, DWCNT and nano-platelets (GPL), has been advanced for application in material science, in MEMS (micro-transducers, micro-actuators, micro-sensor), orthopedic implants, bio-medical instruments and also in the field of advanced transport systems (aerospace engineering, automotive engineering, shipbuilding), light weight armor materials, nuclear power plant, etc. due to their low specific weight, bending stiffness, excellent vibration characteristics and good fatigue properties [22]. Motivated by the potentiality offered by CNTs reinforced composites (CNTRCs) [23,24], and the FGMs concept, in the last decade many researchers investigate on the FG-CNTRC. Shen et al [25,26] studied the nonlinear bending, buckling, and post-buckling behavior of FG-CNTRC plates in thermal environments. Wang et al [27,28] and Abdelhakim et al [29] investigated on nonlinear vibration and bending of FG-CNTRC plates. Liew et al [30] has paid much attention to the linear and nonlinear thermo-mechanical analysis of FG-CNTRC beams, plates and shells, using various theories and

CNTs topology along the grading directions, i.e., uniformly distributed (UD-CNTRC) and functionally graded (FG-◊-CNTRC), (FG-X-CNTRC), (FG-V-CNTRC), and (FG-Λ-CNTRC). Based on three-dimensional theory of elasticity, Alibeigloo and Liew [31] investigated the bending behavior of FG-CNTRC rectangular plates under thermo-mechanical loads. They found, among other things, that stress and deflection at a point were higher for a uniform volume distribution pattern than that at the corresponding point for non-uniform CNT volume distributions. Kumar et al [32] studied the vibration, buckling and bending behavior of FG-MWCNTRC plates using the layer-wise formulation. Phung-Van et al [33] presented an effective formulation based on isogeometric analysis and higher-order shear deformation theory (HSDT) to investigate the static and dynamic behavior of FG-CNTRC plates. The buckling of FG-SWCNTRC rectangular plate subjected to uniaxial and biaxial in-plane mechanical loadings was investigated by Mehrabadi et al. [34] using FSDT. They concluded that CNTRC plates with symmetric distribution profile are the potential alternative to the plates with uniformly distributed (UD) CNTs. Linear vibration using FSDT has been investigated by Zhang et al [35] and Vo-Duy et al [36]. Wang et al [37] investigated free vibration and static bending behavior of FG-GPLRC doubly-curved shallow shells, using HSDT and Navier solution method. Buckling and post buckling of nanocomposite plates having randomly oriented nanotubes under uniaxial compression were studied by Srivastava et al [38], free and forced vibrations of FG-GPLRC by Song et al [39] and bi-axially compressed FG-GPLRC plates by Song et al [40]; thermal post-buckling by Kiani [41]; transient and impact analysis by Lei et al [42], dynamic instability analysis of sandwich plate with CNT reinforced face-sheets is performed by Sankar et al [43], Jam et al [44] studied the low velocity impact response of FG-CNTRC beams in thermal environment, using Timoshenko beam theory, and Yang et al [45] that of spherical shells using FSDT. Lin et al [46] investigated the vibration characteristics of CNTRC beams based on the first (FSDT) and Reddy's third order shear deformation beam theories (TSDT) [47]. Jalali et al [48] studied the buckling of circular sandwich plates with tapered cores and FG-CNTRC face sheets. Static and dynamic analyses of plates resting on Pasternak elastic foundation were performed by Wattanasakulpong et al [49]. Geometrically nonlinear large deformation analysis of internally supported nanocomposite plates subjected to a uniformly distributed load has been investigated by Zhang [50].

Concerning the solution method, Natarajan et al [51] investigated the bending and the free flexural vibration of sandwich plates with CNTRC face-sheets using QUAD-8 shear flexible element developed in Natarajan et al [52]. Sankar et al [43] studied the panel flutter characteristics and the dynamic instability due to in-plane periodic load of sandwich plates with CNTRC face-sheets using an accurate higher-order theory and QUAD-8 shear flexible element developed by Natarajan et al [52]. In Sankar et al [53] the nonlinear dynamic thermal buckling of sandwich spherical and conical shells with CNTRC face-sheets is studied, using three-nodes axisymmetric curved shell element. The effect of nonuniform thermal loading on thermal buckling and free vibration of FG-CNTRC plate has been studied by George

3

et al [54] using the finite element method. The bending analysis of FG-CNTRC plate has been performed by Chavan et al [55] using a C^0 continuity 9-node isoparametric element with seven degrees of freedom per node based on HSDT. Ansari et al [56] examine the effect of uniaxially aligned CNTs on flexural and free vibration analysis of FG-CNTRC plate using a 9-node C^0 continuity isoparametric element with seven degrees of freedom per node and based on a third-order Taylor's series polynomial in the thickness co-ordinate.

Based on the classical shell theory and Galerkin's method, Nguyen Dinh et al [57] studied the linear dynamic response of FG-SWCNTRC truncated conical shells resting on elastic foundations. Moradi-Dastjerdi et at [58] investigated the vibrational behavior (free and forced vibrations, resonance and pulse response) of sandwich plates with FG-CNTR face sheets resting on Pasternak elastic foundation, using a mesh-free method and FSDT. Huang et al. [59] present the nonlinear buckling analysis of FG-GPLRC shallow arches with elastic rotational constraints under uniform radial load. Using 8-node isoparametric plate element with five degrees of freedom per node based on FSDT, Rout et al. [60] investigate the transient response of four types of SWCNTRC plates subjected to low velocity impact. Mehar et al [61] investigated the free vibration analysis of FG-CNTRC plate under elevated thermal environment, using isoparametric finite elements based on HSDT. The buckling of FG-SWCNTRC plates of polygonal planform was investigated by Zhang [62] using FSDT and the element-free IMLS-Ritz method; skew plate was studied by Zhang et al [63,64] and Kiani [63,64]; quadrilateral plate using FSDT element-free method by Zhang et al [65]; annular sector plate under thermal loadings by Ansari et al [66] and elliptical plates [67]. A study of linear free vibrations of FG-CNTRC in thermal environment was given by Lei et al [42,68] using the element-free kp-Ritz method. Mirzaei et al [69] studied the nonlinear free vibration of temperature-dependent sandwich beams with CNTRC face-sheets using the Timoshenko beam theory and the Ritz method with polynomial basis functions. Bhardwaj et al [70] presented nonlinear flexural and dynamic response of CNTRC plates using FSDT and solutions were obtained using Chebyshev polynomials. Selim et al. [71] investigated the vibration behavior of FG-CNTRC plates in a thermal environment using Reddy's TSDT and the element-free kp-Ritz method; nonlinear free vibration of FG-CNTR flat panel with temperature dependent material properties has been studied by Mehar et al [72] using HSDT and finite element method; buckling using the element-free kp-Ritz method by Lei et al [73,74]. In all the above studies, analysis was conducted by considering the plate as an equivalent single layer (with the exception of Kumar et al [32] where the layer-wise formulation has been adopted) with one or few types of volume fraction distribution of CNTs and using Equivalent Single Layer (ESL) theories, such as CPT, FSDT, HSDT theories, coupled with some numerical solution method (Finite element, element-free kp-Ritz method, cell-based smoothed discrete shear gap method by Phung-Van et al [75–79]). Due to inherent constraints in manufacturing processes, fabrication of ideal FG-CNT reinforced structure is extremely difficult. So, the dynamic analysis of CNTRC plate has been extended by considering multi-layer structure and has been performed by layer-wise

theory [32,76]. Previous literature review, although not exhaustive, shows that many ESL theories were used in the analysis of thermo-mechanical structural behavior of FG-CNTRC beams, plates and shells. To the best of the authors knowledge, only few papers use layer-wise [32,76,80] or zigzag theories [43,51,81–83].

Recently, Tessler et al formulated a new zigzag model, known as the Refined Zigzag Theory (RZT) for multilayered and sandwich beams [84–86], plates [87,88] and shells [89]. In the RZT, the FSDT in-plane kinematics is improved with a piecewise linear zigzag function. In Iurlaro et al [90–93] the excellent capabilities of RZT to solve static, dynamic and stability problems for laminate and sandwich plates have been assessed. The RZT does not require the use of fictitious shear correction factors; moreover it is well suited for the formulation of C^0 finite elements, as indicated by [94–96]. In Iurlaro et al. [93], the RZT has been extended to analyse functionally graded sandwich plates. Recently, Di Sciuva and Sorrenti [97] have been performed a deep numerical investigation in order to assess the capabilities of the RZT to analyse functionally graded sandwich plates. They concluded that RZT performs very well and in many cases better than Reddy's TSDT. The present work extends the previous assessment to FG-CNTs sandwich plates.

The paper is organized as follows.

In Sect. 2, the general theory and the governing equations are derived. First, the extended RZT (eRTZ) is presented; based on the eRZT kinematics, the discrete governing equations for bending, free vibration and buckling analysis of functionally graded multilayered composite and sandwich plates are derived directly from the principle of virtual work. The effective material properties (Young's moduli, Poisson's ratios and mass density) of the layer reinforced by CNTs uniaxially aligned along the x_1-direction and functionally graded in the x_3-direction following different distributions (UD-CNT, FGΛ-CNT, FGV-CNT, FG◊-CNT, FGX-CNT) are derived using the extended rule of mixture, under the constraint that the value of CNT volume fraction is the same for the various distributions.

Sect. 3 presents numerical studies. Results concerning bending, free vibration and buckling of functionally graded carbon nanotube (FG-CNTR) sandwich plates are presented. Two stacking sequences are considered: sandwich panels with a homogeneous core and FG-CNTR face-sheets and sandwich panels with homogeneous face-sheets and an FG-CNTR core.

First, convergence analysis results of the Ritz method in conjunctions with orthogonal and non-orthogonal admissible functions are presented and discussed.

Subsequently, in order to validate the predictive capability of the eRZT for the problems at hand, comparative numerical studies are performed using 3D elasticity, whenever available, FSDT (using standard and ad-hoc transverse shear correction factors) and Reddy's TSDT. The numerical assessment confirms the superior predictive capabilities of the eRZT over the traditional FSDT and TSDT, also for FG-CNTR sandwich plates. Finally, a detailed parametric numerical investigation is carried out based on the eRZT. Bending under transverse uniform pressure, free vibration and

buckling loads under uniform in-plane uniaxial and biaxial loadings of FG-CNTR sandwich plates are studied. Numerical results for square and rectangular FG-CNTR sandwich plates of different aspect ratio under various combinations of geometry (core-to-face sheet thickness ratio and plate to thickness ratio), different combination of boundary conditions, CNT volume fraction and thickness-wise topology (UD-CNT, FG∧-CNT, FGV-CNT, FG◊-CNT, FGX-CNT with the same value of CNT volume fraction within the face sheets or the core layers) are presented and discussed in details.

In Sect.4, some conclusions are drawn based on the performed numerical investigations.

In Appendix, the assumed orthogonal and non-orthogonal trial functions used in the Ritz method are discussed, in conjunction with the Gram-Schmidt orthogonalization method.

2 Governing equations

2.1 Geometrical preliminaries

We consider a rectangular multilayered flat plate made of a finite number N of perfectly bonded layers. V is the volume of the plate, h the thickness, a the length and b the width. The thickness of each layer, as well as of the whole plate, is assumed to be constant, and the material of each layer is assumed to be linearly elastic and orthotropic with a plane of elastic symmetry parallel to the reference surface and whose principal orthotropy directions are arbitrarily oriented with respect to the reference frame. The points of the plate are referred to an orthogonal Cartesian co-ordinate system $\mathbf{X} = x_j$ $(j = 1, 2, 3)$, where $\mathbf{x} = x_\alpha$ $(\alpha = 1, 2)$ is the set of in-plane co-ordinates on the reference plane, here chosen to be the middle plane of the plate, and $x_3 \equiv z$, is the co-ordinate normal to the reference plane (Figure 1); the origin of the reference frame is fixed at the center of the middle-plane of the plate, so that, x_1 is defined in the range $x_1 \in \left[-\frac{a}{2}, +\frac{a}{2}\right]$, x_2 in the range $x_2 \in \left[-\frac{b}{2}, +\frac{b}{2}\right]$, and x_3 in the range $x_3 \in \left[-\frac{h}{2}, +\frac{h}{2}\right]$. In the body of paper, also the following nondimensional co-ordinates will be adopted $(\xi_1, \xi_2) = \left(\frac{2x_1}{a}, \frac{2x_2}{b}\right) \in [-1, +1]$.

If not otherwise stated, in the paper the superscript (k) is used to indicate quantities corresponding to the kth layer $(k=1,N)$, whereas the subscript (k) defines quantities corresponding to the kth interface $(k=1,N-1)$ between the k and $(k+1)$ layer. So, in the following, the symbol $(.)_{(k)}$ stands for $(.)$ valued for $x_3 = z_{(k)}$, i.e., at the k-th interface. Also, we use the subscript b and t to indicate the top and bottom surfaces of the plate; specifically, $z_{(0)} = z_b$ and $z_{(N)} = z_t$ denote the co-ordinates of the bottom and top surfaces of the whole plate; thus, $h = z_t - z_b$ is the plate thickness and $h^{(k)} = z_{(k)} - z_{(k-1)}$ $(k = 1, 2, ..., N)$, the thickness of the kth layer (see Figure 1).

The plate is subjected to a transverse load $\bar{q}_z$ applied on the top surface of the plate, and to uniformly distributed in-plane edge loads for unit length, $\bar{P}_{11}$, $\bar{P}_{22}$ and $\bar{P}_{12}$ and boundary transverse loads $\bar{T}_{13}$, $\bar{T}_{23}$, applied along the edges $x_1 = \pm \frac{a}{2}$ and $x_2 = \pm \frac{b}{2}$, respectively (see, Figure 1).

The symbol $(\bullet)_{,i} = \dfrac{\partial(\bullet)}{\partial x_i}$ refers to the derivative of the function $(\bullet)$ with respect to the coordinate x_i, i.e., $(\bullet)_{,i} = \dfrac{\partial(\bullet)}{\partial x_i}$.

In the paper, if not otherwise specified, the Einstenian summation convention over repeated indices is adopted, with Latin indices ranging from 1 to 3, and Greek indices ranging from 1 to 2.

(a)

(b)
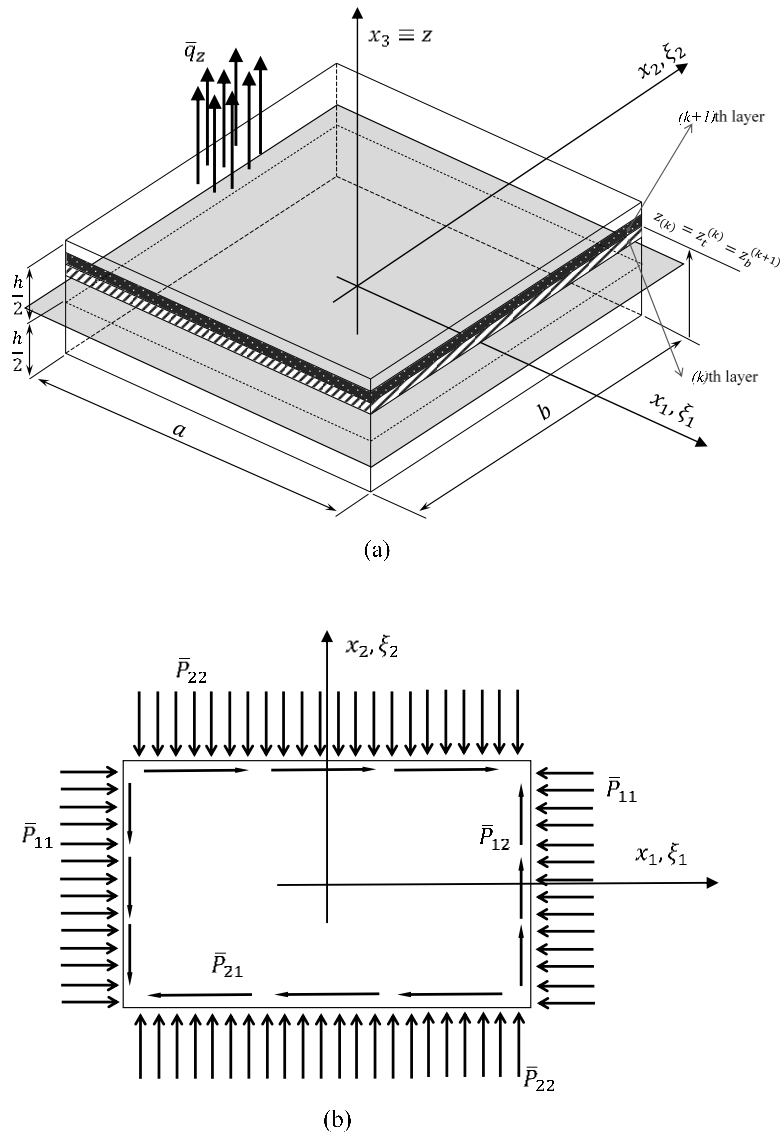
Figure 1. General plate notation: (a) plate geometry and co-ordinate system and layer numbering, (b) in-plane loads.

2.2 Homogenization of material properties

It is assumed that functionally graded carbon nano-tubes reinforced (FG-CNTR) layers are made from a mixture of (10, 10) armchair single-walled carbon nanotubes (SWCNTs) as reinforcement, and a matrix which is assumed to be isotropic and homogeneous from Mirzaei and Kiani [69]. The effective material properties of the two-phase composites, mixture of CNTs and an isotropic polymer, can be estimated according to the modified rule of mixtures (ROM) or the Mori–Tanaka scheme. Due to its simplicity and by taking into consideration that for the problem at hand they give almost identical results, as shown by Lei et al [74], in the present study the modified ROM is used to obtain the equivalent properties of the CNTR layer.

According to the extended ROM, the effective material properties are given by [74]

$$E_{11} = \eta_1 V_{cnt} E_{11}^{cnt} + V_m E^m \tag{1}$$

$$\frac{\eta_2}{E_{22}} = \frac{V_{cnt}}{E_{22}^{cnt}} + \frac{V_m}{E^m} \tag{2}$$

$$\frac{\eta_3}{G_{12}} = \frac{V_{cnt}}{G_{12}^{cnt}} + \frac{V_m}{G^m} \tag{3}$$

$$\nu_{12} = V_{cnt}^* \nu_{12}^{cnt} + V_m \nu^m \tag{4}$$

$$\rho = V_{cnt} \rho^{cnt} + V_m \rho^m \tag{5}$$

In the above equations, $E_{11}^{cnt}, E_{22}^{cnt}$ and G_{12}^{cnt}, ν_{12}^{cnt} and ρ^{cnt} are the Young's moduli, the shear modulus, the Poisson's ratio and the mass density of SWNCTs, respectively; E^m, G^m, ν^m and ρ^m the corresponding quantities of the isotropic matrix phase. The coefficients η_i $(i = 1,2,3)$ are the so-called *efficiency parameters*: they account for the scale-dependent material properties; they are evaluated by matching the effective properties of CNTRC obtained from the molecular dynamic's simulations with those from the rule of mixtures [98]. Furthermore, V_{cnt} and V_m are the volume fractions of CNTs and matrix phase, respectively, which satisfy the condition

$$V_{cnt} + V_m = 1 \tag{6}$$

The mathematical expressions of CNTs volume fractions for the five topologies considered in this paper are given in Table 1, where V_{cnt}^* is given by

$$V_{cnt}^* = \frac{w_{cnt}}{w_{cnt} + \left(\rho^{cnt} / \rho^m\right)\left(1 - w_{cnt}\right)} \tag{7}$$

and w_{cnt} is the mass fraction of the CNTs.

There are five different topologies of CNTR layers investigated in the open literature, i.e., uniformly distributed (UD) and four different functionally graded (FG) cases, namely FG-V, FG-◊, FGX and FG-Λ, this last being the symmetric one of FG-V (Figure 2). In this investigation, all of these topologies are considered for each of the face sheets and cores of FG-CNTR sandwich plates.
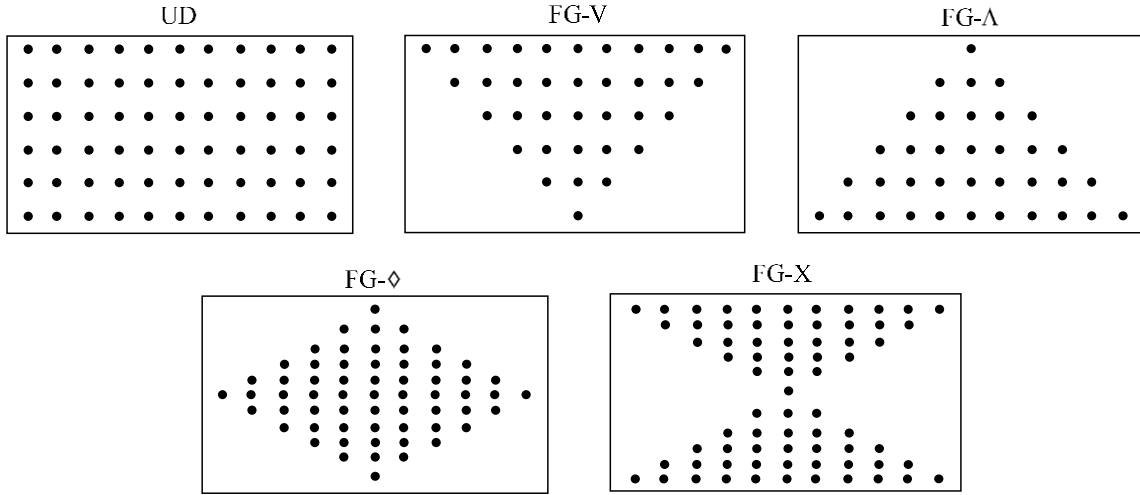
Figure 2. Topologies of FG-CNTR layers

Table 1. Volume fractions of the CNTRC for various distribution as a function of the z-coordinate (layer kth of thickness $h^{(k)}$; reference plane is the middle plane).

CNTs distribution	Volume fraction
UD CNTRC	$V_{cnt}^{(k)}(z) = V_{cnt}^{*(k)}$
FG-V CNTRC	$V_{cnt}^{(k)}(z) = \left(1 + \dfrac{2}{h^{(k)}}\left(z - z_M^{(k)}\right)\right)V_{cnt}^* = \left(1 + \dfrac{2}{h^{(k)}}\left(z - \dfrac{z_t^{(k)} + z_b^{(k)}}{2}\right)\right)V_{cnt}^*$
FG-Λ CNTRC	$V_{cnt}^{(k)}(z) = \left(1 - \dfrac{2}{h^{(k)}}\left(z - z_M^{(k)}\right)\right)V_{cnt}^* = \left(1 - \dfrac{2}{h^{(k)}}\left(z - \dfrac{z_t^{(k)} + z_b^{(k)}}{2}\right)\right)V_{cnt}^*$
FG-X CNTRC	$V_{cnt}^{(k)}(z) = \dfrac{4}{h^{(k)}}\left|z - z_M^{(k)}\right|V_{cnt}^* = \dfrac{4}{h^{(k)}}\left|z - \dfrac{z_t^{(k)} + z_b^{(k)}}{2}\right|V_{cnt}^*$
FG-◊ CNTRC	$V_{cnt}^{(k)}(z) = 2\left(1 - \dfrac{2}{h^{(k)}}\left|z - z_M^{(k)}\right|\right)V_{cnt}^* = 2\left(1 - \dfrac{2}{h^{(k)}}\left|z - \dfrac{z_t^{(k)} + z_b^{(k)}}{2}\right|\right)V_{cnt}^*$

Table 1 gives the volume fractions for the CNT as a function of the z-coordinate for various topologies; $h^{(k)} = z_t^{(k)} - z_b^{(k)}$ and $z_M^{(k)} = \dfrac{z_t^{(k)} + z_b^{(k)}}{2}$ are the thickness and the co-ordinate of the middle plane of the kth layer (here assumed as reference plane). It is easy to check from Table 1 that UD and all of FG types will have the same value of volume fraction of CNTs.

As the effective Poisson ratio depends weakly on position [99], generally, it is assumed that the Poisson's ratio is constant along the thickness. For the other mechanical moduli the following assumptions are made [82]

$$
\begin{aligned}
E_{33} &= E_{22}; \quad G_{13} = G_{23} = G_{12} \\
V_{13} &= V_{12}; \quad V_{31} = V_{21}; \quad V_{32} = V_{23} = V_{21}; \quad V_{21} = \frac{E_{22}}{E_{11}} V_{12}.
\end{aligned}
\tag{8}
$$

Thus, the material characteristics are functions of the volume fractions of CNTs and matrix. By taking into account that Eq. (4) must by satisfied, only one of the two volume fractions could be chosen. Obviously, the volume fraction of CNTs is chosen.

2.3 Kinematics

To take into account layers made up of FGMs, the kinematics of the extended Refined Zigzag Theory (eRZT) [93], is adopted. The theory is based on the superposition of a global (G) first–order kinematics (that of the Mindlin plate theory) and a local (L) layer-wise correction of the in-plane displacements (see, Figure 3). Thus, the displacement field at time t is written in compact matrix format as

$$
\begin{aligned}
\tilde{\mathbf{u}}(x_j, t) &= \mathbf{u}^G(x_j, t) + \mathbf{u}^L(x_j, t) \\
\tilde{u}_3(x_j, t) &= u_3^G(x_j, t)
\end{aligned}
\tag{9}
$$

where

$$
\begin{aligned}
\mathbf{u}^G(x_j, t) &= \mathbf{u}(x_\beta, t) + z\boldsymbol{\theta}(x_\beta, t) \\
u_3^G(x_j, t) &= w(x_\beta, t)
\end{aligned}
\tag{10}
$$

gives the contribution which is continuous with its first derivatives with respect to the z-coordinate and

$$
\mathbf{u}^{L(k)}(x_j, t) = \boldsymbol{\phi}^{(k)}(z)\boldsymbol{\psi}(x_\beta, t)
\tag{11}
$$

gives the contribution to the in-plane displacement which is continuous with respect to z, but with jumps in the first derivative at the interfaces between adjacent layers.

In Eqs. (9)-(11),

$$\tilde{\mathbf{u}}(x_j,t) = \begin{Bmatrix} \tilde{u}_1(x_j,t) \\ \tilde{u}_2(x_j,t) \end{Bmatrix}, \quad \mathbf{u}^G(x_j,t) = \begin{Bmatrix} \tilde{u}_1^G(x_j,t) \\ \tilde{u}_2^G(x_j,t) \end{Bmatrix}, \quad \mathbf{u}^L(x_j,t) = \begin{Bmatrix} \tilde{u}_1^L(x_j,t) \\ \tilde{u}_2^L(x_j,t) \end{Bmatrix} \tag{12}$$

$$\mathbf{u}(x_\beta,t) = \begin{Bmatrix} u_1(x_\beta,t) \\ u_2(x_\beta,t) \end{Bmatrix}, \quad \boldsymbol{\theta}(x_\beta,t) = \begin{Bmatrix} \theta_1(x_\beta,t) \\ \theta_2(x_\beta,t) \end{Bmatrix} \tag{13}$$

$$\boldsymbol{\psi}(x_\beta,t) = \begin{Bmatrix} \psi_1(x_\beta,t) \\ \psi_2(x_\beta,t) \end{Bmatrix}, \quad \boldsymbol{\phi}^{(k)} = \begin{bmatrix} \phi_1^{(k)}(z) & 0 \\ 0 & \phi_2^{(k)}(z) \end{bmatrix} \tag{14}$$

In the previous equations, u_1 and u_2 are the displacements along the x_1- and x_2- axis of a point belonging to the middle plane of the plate; θ_1 and θ_2 are the bending rotation of the normal to the middle surface along the directions $+x_2$ and $-x_1$, respectively, and w is the transverse deflection, assumed to be constant along the thickness. ψ_1 and ψ_2 represent the spatial amplitudes of the zigzag functions $\phi_1^{(k)}$ and $\phi_2^{(k)}$, respectively. It should be noted that FSDT is a special case of the RZT, i.e., RZT reduces to FSDT for $\boldsymbol{u}^{L(k)} = \mathbf{0}$ (see, Eqs. (9) and (10)).
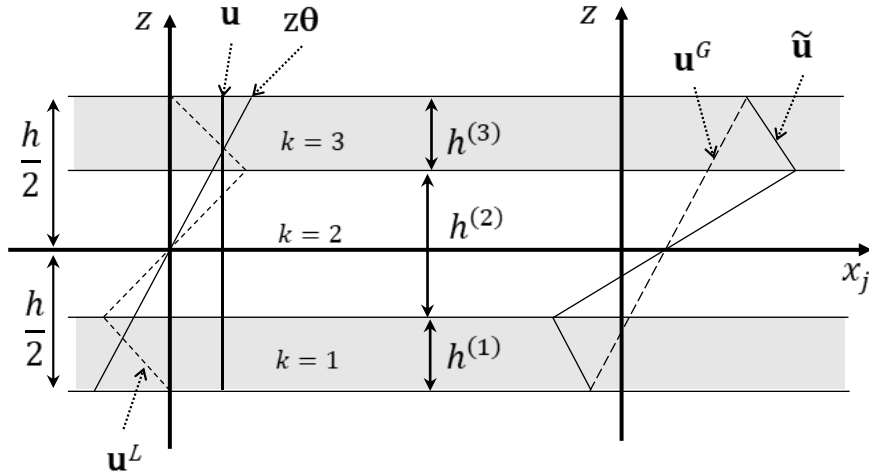
Figure 3. Contributions to the in plane RZT kinematics for a three-layered laminate.

2.4 Strain-displacement relations

The linear strain expressions associated with the displacement field in Eq. (9) are, in compact matrix format,

$$\tilde{\boldsymbol{\varepsilon}}^{(k)} = \boldsymbol{\varepsilon}_m + z\boldsymbol{\varepsilon}_b + \boldsymbol{\Phi}^{(k)}\boldsymbol{\varepsilon}_\phi \tag{15}$$

$$\tilde{\boldsymbol{\gamma}}^{(k)} = \boldsymbol{\gamma}^{(0)} + \boldsymbol{\phi}_{,3}^{(k)}\boldsymbol{\psi} \tag{16}$$

where

$$\boldsymbol{\varepsilon}^{(k)} = \begin{Bmatrix} \tilde{\varepsilon}_{11} \\ \tilde{\varepsilon}_{22} \\ \tilde{\gamma}_{12} \end{Bmatrix}^{(k)} = \begin{Bmatrix} \tilde{u}_{1,1} \\ \tilde{u}_{2,2} \\ \tilde{u}_{1,2} + \tilde{u}_{2,1} \end{Bmatrix}, \quad \boldsymbol{\varepsilon}_m = \begin{Bmatrix} u_{1,1} \\ u_{2,2} \\ u_{1,2} + u_{2,1} \end{Bmatrix}, \quad \boldsymbol{\varepsilon}_b = \begin{Bmatrix} \theta_{1,1} \\ \theta_{2,2} \\ \theta_{1,2} + \theta_{2,1} \end{Bmatrix} \tag{17}$$

$$\boldsymbol{\varepsilon}_\phi = \begin{Bmatrix} \psi_{1,1} \\ \psi_{2,1} \\ \psi_{1,2} \\ \psi_{2,2} \end{Bmatrix}, \quad \boldsymbol{\Phi}^{(k)} = \begin{bmatrix} \phi_1^{(k)} & 0 & 0 & 0 \\ 0 & 0 & 0 & \phi_2^{(k)} \\ 0 & \phi_2^{(k)} & \phi_1^{(k)} & 0 \end{bmatrix} \tag{18}$$

$$\tilde{\boldsymbol{\gamma}}^{(k)} \begin{Bmatrix} \tilde{\gamma}_{13} \\ \tilde{\gamma}_{23} \end{Bmatrix}^{(k)} = \begin{Bmatrix} u_{1,3} + w_{,1} \\ u_{2,3} + w_{,2} \end{Bmatrix}^{(k)}, \quad \boldsymbol{\gamma}^{(0)} = \begin{Bmatrix} \theta_1 + w_{,1} \\ \theta_2 + w_{,2} \end{Bmatrix} \tag{19}$$

For the kth layer of thickness $h^{(k)}$, the following expressions hold for the refined zigzag functions [88,93]:

$$\phi_1^{(k)}(z) = \left(z + \frac{h}{2}\right)\left(\frac{G_4}{Q_{44}^{(k)}(z)} - 1\right) + \sum_{q=2}^{k} h^{(q-1)}\left(\frac{G_4}{Q_{44}^{(q-1)}(z)} - \frac{G_4}{Q_{44}^{(k)}(z)}\right)$$
$$\phi_2^{(k)}(z) = \left(z + \frac{h}{2}\right)\left(\frac{G_5}{Q_{55}^{(k)}(z)} - 1\right) + \sum_{q=2}^{k} h^{(q-1)}\left(\frac{G_5}{Q_{55}^{(q-1)}(z)} - \frac{G_5}{Q_{55}^{(k)}(z)}\right) \qquad (k = 1, \dots, N) \tag{20}$$

where

$$G_j = \left(\frac{1}{h} \sum_{k=1}^{N} \int_{z_b^{(k)}}^{z_t^{(k)}} \frac{dz}{Q_{jj}^{(k)}(z)}\right)^{-1} \qquad j = 4,5 \tag{21}$$

and $Q_{jj}^{(k)}(z)$ is the transverse shear stiffness modulus of the kth layer (see Section 2.5).

Eqs. (20) and (21) show that the *refined zigzag functions* $\phi_\alpha^{(k)}$ are *a priori* known piecewise continuous functions of z, vanishing on the bottom $\left(z = -\frac{h}{2}\right)$ and top $\left(z = +\frac{h}{2}\right)$ surfaces of the plate (see, Figure 3). Note that, contrary to what happens for the traditional multilayered composite and sandwich structures where $\phi_\alpha^{(k)}$ is a piecewise linear function of the z-coordinate [88], for multilayered structures with layers made of functionally graded materials, $\phi_\alpha^{(k)}$ is a piecewise-non-linear function whose shape is regulated by the grading law of the transverse shear stiffness [93]. Thus, the transverse shear strains $\gamma_{\alpha3}^{(k)}$ are nonlinear functions of z within each layer (see, Eq. 16).

2.5 Stress-strain relations

The constitutive equations for a functionally graded layer are[2], in compact matrix format,

$$\tilde{\boldsymbol{\sigma}}_p^{(k)} = \bar{\mathbf{Q}}_p^{(k)} \tilde{\boldsymbol{\varepsilon}}^{(k)} \tag{22}$$

---

[2] In the present plate theory it is assumed $\sigma_{33} = 0$.

$$\tilde{\boldsymbol{\sigma}}_t^{(k)} = \overline{\mathbf{Q}}_t^{(k)} \tilde{\boldsymbol{\gamma}}^{(k)} \tag{23}$$

where

$$\tilde{\boldsymbol{\sigma}}_p^{(k)} = \begin{Bmatrix} \tilde{\sigma}_{11} \\ \tilde{\sigma}_{22} \\ \tilde{\sigma}_{12} \end{Bmatrix}^{(k)} \quad , \quad \tilde{\boldsymbol{\sigma}}_t^{(k)} = \begin{Bmatrix} \tilde{\sigma}_{13} \\ \tilde{\sigma}_{23} \end{Bmatrix}^{(k)} \tag{24}$$

$$\overline{\mathbf{Q}}_p^{(k)} = \begin{bmatrix} \overline{Q}_{11} & \overline{Q}_{12} & \overline{Q}_{16} \\ \overline{Q}_{12} & \overline{Q}_{22} & \overline{Q}_{26} \\ \overline{Q}_{16} & \overline{Q}_{26} & \overline{Q}_{66} \end{bmatrix}^{(k)} \quad , \quad \overline{\mathbf{Q}}_t^{(k)} = \begin{bmatrix} \overline{Q}_{44} & \overline{Q}_{45} \\ \overline{Q}_{45} & \overline{Q}_{55} \end{bmatrix}^{(k)} \tag{25}$$

In Eq. (25) $\overline{Q}_{ij}^{(k)}(z)$ (i,j=1,2,6) and and $\overline{Q}_{ij}^{(k)}(z)$ (i,j=4,5) are the plane stress transformed stiffness moduli of the kth layer, that are functions of the z-coordinate.

2.6 Discrete equations of motion

The discretized equations of motion are obtained from the dynamic version of the principle of virtual displacements (D'Alembert principle)

$$\delta U - \delta W_{ext} = \delta W_{in} \tag{26}$$

where

$$\delta U = \int_{-a/2}^{+a/2} \int_{-b/2}^{+b/2} \left\langle \delta \tilde{\boldsymbol{\varepsilon}}_p^T \tilde{\boldsymbol{\sigma}}_p + \delta \tilde{\boldsymbol{\gamma}}^T \tilde{\boldsymbol{\sigma}}_t \right\rangle dx_1 dx_2 \tag{27}$$

is the virtual variation of the work done by the internal forces (stress);

$$\delta W_{in} = -\int_{-a/2}^{+a/2} \int_{-b/2}^{+b/2} \left\langle \rho \left(\ddot{\tilde{\mathbf{u}}}^T \delta \tilde{\mathbf{u}} + \ddot{\tilde{u}}_3 \delta w \right) \right\rangle dx_1 dx_2 \tag{28}$$

is the virtual variation of the work done by the inertia forces, and δW_{ex} is the virtual variation of the work done by the applied forces. Obviously,

$$\delta W_{ex} = 0 \tag{29}$$

for free vibration. Moreover,

$$\delta W_{ex} = \int_{-a/2}^{+a/2} \int_{-b/2}^{+b/2} \bar{q}_3 \, \delta w \, dx_1 dx_2 +$$

$$+ \int_{-a/2}^{+a/2} \left(\bar{T}_{23}(x_1, -\frac{b}{2}, t) \delta w(x_1, -\frac{b}{2}, t) + \bar{T}_{23}(x_1, \frac{b}{2}, t) \delta w(x_1, \frac{b}{2}, t) \right) dx_1 + \tag{30}$$

$$+ \int_{-b/2}^{+b/2} \left(\bar{T}_{13}(-\frac{a}{2}, x_2, t) \delta w(-\frac{a}{2}, x_2, t) + \bar{T}_{13}(\frac{a}{2}, x_2, t) \delta w(\frac{a}{2}, x_2, t) \right) dx_2$$

for bending, and

$$\delta W_{ex} = \int_{-a/2}^{+a/2} \int_{-b/2}^{+b/2} \left(\begin{bmatrix} \bar{P}_{11} & \bar{P}_{12} \\ \bar{P}_{21} & \bar{P}_{22} \end{bmatrix} \begin{Bmatrix} w_{,1} \\ w_{,2} \end{Bmatrix} \right)^T \delta \begin{Bmatrix} w_{,1} \\ w_{,2} \end{Bmatrix} dx_1 dx_2 \tag{31}$$

for buckling under normal and shear in-plane loads.

In writing Eq. (30) it is assumed that for bending analysis, the plate is subjected to a transverse load $\bar{q}_3$ applied on the top surface of the plate, and to a boundary transverse loads per unit length $\bar{T}_{\alpha 3}$ ($\alpha = 1, 2$) applied on the edge parallel to x_α-axis. For buckling analysis, Eq. (31), the plate is assumed to be loaded by distributed in-plane normal and shear loads for unit length, $\bar{P}_{\alpha\beta}$ applied on the edges (see, Figure 1(b)). It is also assumed that the top and bottom surfaces of the plate are free of shear tractions.

In the previous equations, $\rho(x_3)$ is the material mass density; the overdot indicates differentiation with respect to the time, and an overbar the prescribed value of a quantity. All other symbols have been defined above. Moreover,

$$\langle \bullet \rangle = \sum_{s=1}^{N} \int_{x_3(s-1)}^{x_3(s)} (\bullet) dx_3$$

and δ is the variational operator.

Substitution of Eqs. (9), (15), (16) into Eqs. (27) and (28), yields

$$\delta U = \int_{-a/2}^{+a/2} \int_{-b/2}^{+b/2} \delta \mathbf{e}^T \mathbf{R} dx_1 dx_2 \tag{32}$$

where

$$\mathbf{R}^T = \begin{bmatrix} \mathbf{N}^T & \mathbf{M}^T & \mathbf{M}_b^{(\phi)T} & \mathbf{T}^T & \mathbf{T}^{(\phi)T} \end{bmatrix} \tag{33}$$

$$\mathbf{e}^T = \begin{bmatrix} \boldsymbol{\varepsilon}_m^T & \boldsymbol{\varepsilon}_b^T & \boldsymbol{\varepsilon}_\phi^T & \boldsymbol{\gamma}^{(0)T} & \boldsymbol{\psi}^T \end{bmatrix} \tag{34}$$

In Eq. (33) the following force and moment stress resultants for unit length have been introduced

14

$$\left(\mathbf{N},\mathbf{M},\mathbf{M}_b^{(\phi)}\right) = \left(\left\{\begin{matrix} N_{11} \\ N_{22} \\ N_{12} \end{matrix}\right\}, \left\{\begin{matrix} M_{11} \\ M_{22} \\ M_{12} \end{matrix}\right\}, \left\{\begin{matrix} M_{11}^{(\phi)} \\ M_{21}^{(\phi)} \\ M_{12}^{(\phi)} \\ M_{22}^{(\phi)} \end{matrix}\right\}\right) = \left\langle \left(1, z, \begin{bmatrix} \phi_1^{(k)} & 0 & 0 \\ 0 & 0 & \phi_2^{(k)} \\ 0 & 0 & \phi_1^{(k)} \\ 0 & \phi_2^{(k)} & 0 \end{bmatrix}\right)\left\{\begin{matrix} \tilde{\sigma}_{11} \\ \tilde{\sigma}_{22} \\ \tilde{\sigma}_{12} \end{matrix}\right\}\right\rangle \tag{35}$$

$$\left(\mathbf{T},\mathbf{T}^{(\phi)}\right) = \left(\left\{\begin{matrix} T_1 \\ T_2 \end{matrix}\right\}, \left\{\begin{matrix} T_1^{(\phi)} \\ T_2^{(\phi)} \end{matrix}\right\}\right) = \left\langle 1, \begin{bmatrix} \phi_{1,3}^{(k)} & 0 \\ 0 & \phi_{2,3}^{(k)} \end{bmatrix}\left\{\begin{matrix} \tilde{\sigma}_{13} \\ \tilde{\sigma}_{23} \end{matrix}\right\}\right\rangle \tag{36}$$

The **plate constitutive relations** are derived by using Eqs. (15) and (16) with Eqs. (22) and (23) into Eqs. (35) and (36), and integrating over the plate thickness. In matrix format they read

$$\mathbf{R} = \mathbf{S}\mathbf{e} \tag{37}$$

where

$$\mathbf{S} = \begin{bmatrix} \mathbf{A} & \mathbf{B} & \mathbf{A}_\phi & \mathbf{0} & \mathbf{0} \\ \mathbf{B} & \mathbf{D} & \mathbf{B}_\phi & \mathbf{0} & \mathbf{0} \\ \mathbf{A}_\phi^T & \mathbf{B}_\phi^T & \mathbf{D}_\phi & \mathbf{0} & \mathbf{0} \\ \mathbf{0} & \mathbf{0} & \mathbf{0} & \mathbf{A}_t & \mathbf{B}_t^\phi \\ \mathbf{0} & \mathbf{0} & \mathbf{0} & \mathbf{B}_t^{\phi T} & \mathbf{D}_t^\phi \end{bmatrix} \tag{38}$$

$$\left(\mathbf{A},\mathbf{B},\mathbf{D}\right) = \left\langle (1, z, z^2)\bar{\mathbf{Q}}_p \right\rangle, \quad \left(\mathbf{A}_\phi, \mathbf{B}_\phi, \mathbf{D}_\phi\right) = \left\langle \left(1, z, \mathbf{\Phi}^T\right)\bar{\mathbf{Q}}_p \mathbf{\Phi} \right\rangle$$
$$\left(\mathbf{A}_t, \mathbf{B}_t^\phi\right) = \left\langle \left(1, \boldsymbol{\phi}_{,3}^{(k)}\right)\bar{\mathbf{Q}}_t \right\rangle, \quad \mathbf{D}_t^\phi = \left\langle \boldsymbol{\phi}_{,3}^{(k)\mathrm{T}}\mathbf{Q}_t \boldsymbol{\phi}_{,3}^{(k)} \right\rangle \tag{39}$$

The virtual variation of the work done by the inertia forces reads

$$\delta W_{in} = -\int_{-a/2}^{+a/2}\int_{-b/2}^{+b/2}\left\langle \rho \delta \tilde{u}_i^T \ddot{\tilde{u}}_i \right\rangle dx_1 dx_2 = -\int_{-a/2}^{+a/2}\int_{-b/2}^{+b/2}\left\langle \rho\left(\delta \tilde{\mathbf{u}}^T \ddot{\tilde{\mathbf{u}}} + \delta \tilde{u}_3 \ddot{\tilde{u}}_3\right)\right\rangle dx_1 dx_2$$
$$= -\int_{-a/2}^{+a/2}\int_{-b/2}^{+b/2}\delta \mathbf{d}^T \mathbf{m}\ddot{\mathbf{d}} \, dx_1 dx_2 \tag{40}$$

where

$$\mathbf{d} = \left\{\begin{matrix} u_1 \\ u_2 \\ \theta_1 \\ \theta_2 \\ \psi_1 \\ \psi_2 \\ w \end{matrix}\right\}; \quad \mathbf{m} = \begin{bmatrix} m^{(0)} & 0 & m^{(1)} & 0 & m_1^{(0)} & 0 & 0 \\ 0 & m^{(0)} & 0 & m^{(1)} & 0 & m_2^{(0)} & 0 \\ m^{(1)} & 0 & m^{(2)} & 0 & m_1^{(1)} & 0 & 0 \\ 0 & m^{(1)} & 0 & m^{(2)} & 0 & m_2^{(1)} & 0 \\ m_1^{(0)} & 0 & m_1^{(1)} & 0 & m_1^{(2)} & 0 & 0 \\ 0 & m_1^{(0)} & 0 & m_2^{(1)} & 0 & m_2^{(2)} & 0 \\ 0 & 0 & 0 & 0 & 0 & 0 & m^{(0)} \end{bmatrix} \tag{41}$$

$$\left(m^{(0)}, m^{(1)}, m^{(2)}, m_\alpha^{(0)}, m_\alpha^{(1)}, m_\alpha^{(2)} \right) = \left\langle \rho \left(1, z, z^2, \phi_\alpha^{(k)}, z\phi_\alpha^{(k)}, z\phi_\alpha^{(k)2} \right) \right\rangle \tag{42}$$

Due to the difficulty to obtain closed form solutions, we search for an approximate solution. To do this, the differential

problem is transformed into an algebraic one (discretized problem) using the Ritz method and the D'Alembert principle.

Let us expand the unknown functions in the form,

$$\hat{f}\left(\xi_1, \xi_2, t \right) = \sum_{m=1}^{M(f)} C_m^{(f)}(t) g_m^{(f)} \left(\xi_1, \xi_2 \right) = \mathbf{g}^{(f)T} \mathbf{C}^{(f)} \tag{43}$$

where $\hat{f}\left(\xi_1, \xi_2, t \right)$ stands for $\hat{u}_\alpha \left(\xi_1, \xi_2, t \right)$, $\hat{w}\left(\xi_1, \xi_2, t \right)$, $\hat{\theta}_\alpha \left(\xi_1, \xi_2, t \right)$ and $\hat{\psi}_\alpha \left(\xi_1, \xi_2, t \right)$ ($\alpha = 1, 2$), respectively. In Eq.

(43), $C_m^{(f)}(t)$ are unknown coefficients (generalized coordinates) to be varied, and $g_m^{(f)}\left(\xi_1, \xi_2 \right)$ are the approximating

functions. In the Ritz method [32,100] these functions must be admissible functions, i.e., they must not violate the

prescribed or geometric boundary conditions and should also be linearly independent and complete.

Appendix gives details of the admissible functions used in this work.

Thus, by taking into account Eqs. (15), (16), (41) and (43), yields

$$\mathbf{d} = \mathbf{GC} \tag{44}$$

$$\mathbf{e} = \mathbf{G}_\nabla \mathbf{C} \tag{45}$$

where (T stands for transpose)

$$\mathbf{C}^T = \begin{bmatrix} \mathbf{C}_{u_1}^T & \mathbf{C}_{u_2}^T & \mathbf{C}_{\theta_1}^T & \mathbf{C}_{\theta_2}^T & \mathbf{C}_{\psi_1}^T & \mathbf{C}_{\psi 2}^T & \mathbf{C}_w^T \end{bmatrix}; \quad \mathbf{G} = \begin{bmatrix} \mathbf{g}^{u_1 T} & \mathbf{0} & \mathbf{0} & \mathbf{0} & \mathbf{0} & \mathbf{0} & \mathbf{0} \\ \mathbf{0} & \mathbf{g}^{u_2 T} & \mathbf{0} & \mathbf{0} & \mathbf{0} & \mathbf{0} & \mathbf{0} \\ \mathbf{0} & \mathbf{0} & \mathbf{g}^{\theta_1 T} & \mathbf{0} & \mathbf{0} & \mathbf{0} & \mathbf{0} \\ \mathbf{0} & \mathbf{0} & \mathbf{0} & \mathbf{g}^{\theta_2 T} & \mathbf{0} & \mathbf{0} & \mathbf{0} \\ \mathbf{0} & \mathbf{0} & \mathbf{0} & \mathbf{0} & \mathbf{g}^{\psi_1 T} & \mathbf{0} & \mathbf{0} \\ \mathbf{0} & \mathbf{0} & \mathbf{0} & \mathbf{0} & \mathbf{0} & \mathbf{g}^{\psi_2 T} & \mathbf{0} \\ \mathbf{0} & \mathbf{0} & \mathbf{0} & \mathbf{0} & \mathbf{0} & \mathbf{0} & \mathbf{g}^{w T} \end{bmatrix} \tag{46}$$

$$\mathbf{G}_\nabla^T = \begin{bmatrix} \mathbf{g}_{,1}^{u_1 T} & \mathbf{0} & \mathbf{g}_{,2}^{u_2 T} & \mathbf{0} & \mathbf{0} & \mathbf{0} & \mathbf{0} & \mathbf{0} & \mathbf{0} & \mathbf{0} & \mathbf{0} & \mathbf{0} & \mathbf{0} & \mathbf{0} \\ \mathbf{0} & \mathbf{g}_{,2}^{u_2 T} & \mathbf{g}_{,1}^{u_1 T} & \mathbf{0} & \mathbf{0} & \mathbf{0} & \mathbf{0} & \mathbf{0} & \mathbf{0} & \mathbf{0} & \mathbf{0} & \mathbf{0} & \mathbf{0} & \mathbf{0} \\ \mathbf{0} & \mathbf{0} & \mathbf{0} & \mathbf{g}_{,1}^{\theta_1 T} & \mathbf{0} & \mathbf{g}_{,2}^{\theta_2 T} & \mathbf{0} & \mathbf{0} & \mathbf{0} & \mathbf{0} & \mathbf{g}^{\theta_1 T} & \mathbf{0} & \mathbf{0} & \mathbf{0} \\ \mathbf{0} & \mathbf{0} & \mathbf{0} & \mathbf{0} & \mathbf{g}_{,2}^{\theta_2 T} & \mathbf{g}_{,1}^{\theta_1 T} & \mathbf{0} & \mathbf{0} & \mathbf{0} & \mathbf{0} & \mathbf{0} & \mathbf{g}^{\theta_2 T} & \mathbf{0} & \mathbf{0} \\ \mathbf{0} & \mathbf{0} & \mathbf{0} & \mathbf{0} & \mathbf{0} & \mathbf{0} & \mathbf{g}_{,1}^{\psi_1 T} & \mathbf{0} & \mathbf{g}_{,2}^{\psi_1 T} & \mathbf{0} & \mathbf{0} & \mathbf{0} & \mathbf{g}^{\psi_1 T} & \mathbf{0} \\ \mathbf{0} & \mathbf{0} & \mathbf{0} & \mathbf{0} & \mathbf{0} & \mathbf{0} & \mathbf{0} & \mathbf{g}_{,1}^{\psi_2 T} & \mathbf{0} & \mathbf{g}_{,2}^{\psi_2 T} & \mathbf{0} & \mathbf{0} & \mathbf{0} & \mathbf{g}^{\psi_2 T} \\ \mathbf{0} & \mathbf{0} & \mathbf{0} & \mathbf{0} & \mathbf{0} & \mathbf{0} & \mathbf{0} & \mathbf{0} & \mathbf{0} & \mathbf{0} & \mathbf{g}_{,1}^{w T} & \mathbf{g}_{,2}^{w T} & \mathbf{0} & \mathbf{0} \end{bmatrix} \tag{47}$$

Substituting relations (44) and (45) into Eqs. (29)-(32) and (40), taking into account that the virtual variations are arbitrary independent variations, d'Alembert principle yields the following *discretized set of governing equations*

$$\mathbf{M}\ddot{\mathbf{C}}+\left(\mathbf{K}-\lambda\mathbf{K}_G\right)\mathbf{C}=\mathbf{P} \tag{48}$$

where

$$\mathbf{M}=\int_{-a/2}^{+a/2}\int_{-b/2}^{+b/2}\mathbf{G}^T\mathbf{m}\mathbf{G}dx_1dx_2 \tag{49}$$

is the geometric stiffness matrix;

$$\mathbf{K}=\int_{-a/2}^{+a/2}\int_{-b/2}^{+b/2}\mathbf{G}_\Delta^T\begin{bmatrix}\mathbf{A}&\mathbf{B}&\mathbf{A}^\phi&\mathbf{0}&\mathbf{0}\\\mathbf{B}&\mathbf{D}&\mathbf{B}^\phi&\mathbf{0}&\mathbf{0}\\\mathbf{A}^{\phi T}&\mathbf{B}^{\phi T}&\mathbf{D}^\phi&\mathbf{0}&\mathbf{0}\\\mathbf{0}&\mathbf{0}&\mathbf{0}&\mathbf{A}_t&\mathbf{B}_t^\phi\\\mathbf{0}&\mathbf{0}&\mathbf{0}&\mathbf{B}_t^{\phi T}&\mathbf{D}_t^\phi\end{bmatrix}\mathbf{G}_\Delta dx_1dx_2 \tag{50}$$

is the stiffness matrix;

$$\mathbf{K}_G=\begin{bmatrix}0&0&0&0&0&0&0\\0&0&0&0&0&0&0\\0&0&0&0&0&0&0\\0&0&0&0&0&0&0\\0&0&0&0&0&0&0\\0&0&0&0&0&0&0\\0&0&0&0&0&0&\mathbf{k}_G\end{bmatrix}\quad\text{with}\quad\mathbf{k}_G=\int_{-a/2}^{a/2}\int_{-b/2}^{b/2}\begin{bmatrix}\mathbf{g}_{,1}^w&\mathbf{g}_{,2}^w\end{bmatrix}\begin{bmatrix}1&r_{12}\\r_{12}&r_2\end{bmatrix}\begin{bmatrix}\mathbf{g}_{,1}^{wT}\\\mathbf{g}_{,1}^{wT}\end{bmatrix}dx_1dx_2 \tag{51}$$

$\mathbf{K}_G$ is the geometric stiffness matrix and λ is the buckling load parameter,

$$\lambda=\bar{P}_{11},\quad r_{11}=\frac{\bar{P}_{22}}{\bar{P}_{11}},\quad r_{12}=\frac{\bar{P}_{12}}{\bar{P}_{11}} \tag{52}$$

In Eq. (48),

$$\mathbf{P}=\mathbf{0} \tag{53}$$

for free vibration;

$$\mathbf{P}^T=\int_{-a/2}^{+a/2}\int_{-b/2}^{+b/2}\lfloor 0\quad 0\quad 0\quad 0\quad 0\quad 0\quad \bar{p}_3\rfloor\mathbf{G}dx_1dx_2+\int_{\Gamma_p}\lfloor 0\quad 0\quad 0\quad 0\quad 0\quad 0\quad \bar{T}_3\rfloor\mathbf{G}d\Gamma \tag{54}$$

where

$$\int_{\Gamma_p} \overline{T_3} \, \mathbf{G} d\Gamma = \int_{-a/2}^{+a/2} \left(\overline{T}_{23}(x_1, -\frac{b}{2}) \mathbf{g}^w(x_1, -\frac{b}{2}) + \overline{T}_{23}(x_1, \frac{b}{2}) \mathbf{g}^w(x_1, \frac{b}{2}) \right) dx_1 +$$

$$+ \int_{-b/2}^{+b/2} \left(\overline{T}_{13}(-\frac{a}{2}, x_2) \mathbf{g}^w(-\frac{a}{2}, x_2) + \overline{T}_{13}(\frac{a}{2}, x_2) \mathbf{g}^w(\frac{a}{2}, x_2) \right) dx_2 \tag{55}$$

$$= \frac{a}{2} \int_{-1}^{+1} \left(\overline{T}_{23}(\xi, -1) \mathbf{g}^w(\xi, -1) + \overline{T}_{23}(\xi, 1) \mathbf{g}^w(\xi, 1) \right) d\xi +$$

$$+ \frac{b}{2} \int_{-1}^{+1} \left(\overline{T}_{13}(-1, \eta) \mathbf{g}^w(-1, \eta) + \overline{T}_{13}(1, \eta) \mathbf{g}^w(1, \eta) \right) d\eta$$

for bending.

3 Numerical results and discussion

In this Section to assess the Ritz method using Gram-Schmidt orthogonal polynomials (GS polynomials) and non-orthogonal polynomials, a convergence analysis is presented to predict maximum deflection and natural frequencies. Then two types of sandwich plates are taken into consideration (see Figure 4): a sandwich plate with FG-CNTRC face-sheet and orthotropic core (Type A), a sandwich plate with piezoelectric face-sheets and FG-CNTRC core (Type B).
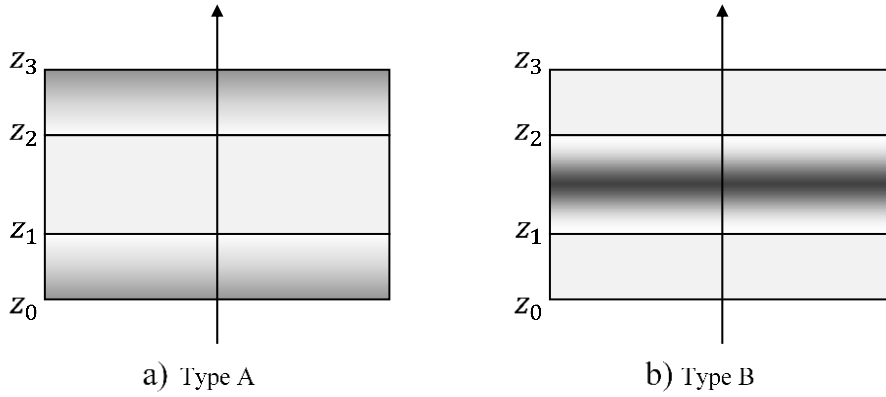
Figure 4. Configuration of functionally graded sandwich plates: (a) Type A, functionally graded face-sheets and homogeneous core; (b) Type B, homogeneous face-sheets and functionally graded core.

In this analysis only the mechanical effect of piezoelectric materials will be considered. Table 2 lists the stacking sequences for the various plates considered. Mechanical material properties for face-sheet and core are listed in Table 3 and Table 4, respectively ([26,73,90,95,101,102]). Table 5 gives the values of volume fraction of CNTs commonly adopted for poly{(mphenylenevinylene)-co-[(2,5-dioctoxy-p-phenylene) vinylene]} (PmPV) matrix and the corresponding efficiency parameters [73]. In Table 6 the efficiency parameters for Poly (methyl methacrylate) (PMMA) matrix and CNTs reinforcement [26] are listed. For this second arrangement of polymeric matrix and CNTs reinforcement (PMMA/CNT), the shear moduli derived from mixture rules are obtained assuming $G_{13} = G_{12}$ and $G_{23} = 1.2G_{12}$.

Table 2. Laminate stacking sequences (from bottom to top surface)

Laminate	Normalized Thickness $h^{(k)}/h$	Lamina materials	Lamina orientation [°]
L1	(0.5/0.5)	A/A	(0/90)
L2	(0.1/0.7/0.2)	F1/N/Q	(0/Core/0)
L3	(0.5/0.5/10/0.5/0.5)	F2/F2/C4/F2/F2	(0/90/Core/0/90)
L4a	Variable (See Table 9)	FG(M1/CNT)/T/ FG(M1/CNT)	(0/Core/0)
L4b	Variable (See Table 14)	FG(M1/CNT)/T/ FG(M1/CNT)	(0/Core/0)
L5a	(0.1667/0.6667/0.1667)	FG(M1/CNT)/T/ FG(M1/CNT)	(0/Core/0)
L5b	(0.125/0.75/0.125)	FG(M1/CNT)/T/ FG(M1/CNT)	(0/Core/0)
L6a	(0.1/0.8/0.1)	PZT-4/FG(M2/CNT)/PZT-4	(0/Core/0)
L6b	(0.1/0.8/0.1)	PZT-5A/FG(M2/CNT)/PZT-5A	(0/Core/0)
L7	(0.1429/0.7143/0.1429)	FG(M1/CNT)/D/ FG(M1/CNT)	(0/Core/0)

Table 3. Mechanical properties of isotropic and orthotropic materials. The Young's moduli, $E_i^{(k)}$, and the shear moduli, $G_{ij}^{(k)}$, are expressed in GPa; the density $\rho^{(k)}$ is expressed in kg/m^3.

	Orthotropic Materials							Isotropic Materials	
	A	F_1	F_2	Q	CNT	PZT-4	PZT-5A	M1 (PMMA)	M2 (PmPV)
$E_1^{(k)}$	157.9	50	131	525	5646.6	81.3	61	2.5	2.1
$E_2^{(k)}$	9.584	10	10.34	21	7080.0	81.3	61	2.5	2.1
$E_3^{(k)}$	9.584	10	10.34	21	-	64.5	53.2	2.5	2.1
$\nu_{12}^{(k)}$	0.32	0.25	0.22	0.25	0.175	0.329	0.35	0.34	0.34
$\nu_{13}^{(k)}$	0.32	0.25	0.22	0.25	-	0.432	0.38	0.34	0.34
$\nu_{23}^{(k)}$	0.49	0.25	0.49	0.25	-	0.432	0.38	0.34	0.34
$G_{12}^{(k)}$	5.930	5	6.895	10.5	1944.5	25.6	22.5	0.9328	0.9328
$G_{13}^{(k)}$	5.930	5	6.205	10.5	-	25.6	21.1	0.9328	0.9328
$G_{23}^{(k)}$	3.227	5	6.895	10.5	-	30.6	21.1	0.9328	0.9328
$\rho^{(k)}$	-	-	1627	-	1400	7600	-	1150	1150

Table 4. Mechanical properties of core materials. The Young's moduli, $E_i^{(k)}$, and the shear moduli, $G_{ij}^{(k)}$, are expressed in GPa; the density $\rho^{(k)}$ is expressed in kg/m^3.

	Orthotropic Materials	Isotropic Materials		
	N	T (Ti-6Al-4V)	C_4	D
$E_1^{(k)}$	10^{-5}	105.7	6.89 x 10^{-3}	0.076775
$E_2^{(k)}$	10^{-5}	105.7	6.89 x 10^{-3}	0.076775
$E_3^{(k)}$	75.85 x 10^{-3}	105.7	6.89 x 10^{-3}	0.076775
$\nu_{12}^{(k)}$	0.01	0.29	0	0.32
$\nu_{13}^{(k)}$	0.01	0.29	0	0.32
$\nu_{23}^{(k)}$	0.01	0.29	0	0.32
$G_{12}^{(k)}$	22.5 x 10^{-3}	40.97	3.45 x 10^{-3}	0.01445
$G_{13}^{(k)}$	22.5 x 10^{-3}	40.97	3.45 x 10^{-3}	0.01445
$G_{23}^{(k)}$	22.5 x 10^{-3}	40.97	3.45 x 10^{-3}	0.01445
$\rho^{(k)}$	-	4429	97	100

Table 5. Efficiency parameters for PmPV/CNT (T=300 K) composite for various values of volume fractions [73].

V_{cnt}^*	η_1	η_2	η_3
0.11	0.149	0.934	0.934
0.14	0.150	0.941	0.941
0.17	0.149	1.381	1.381

Table 6. Efficiency parameters for PMMA/CNT (T=300 K) composite for various values of volume fractions [26].

CNT-PMMA			
V_{cnt}^*	η_1	η_2	η_3
0.12	0.137	1.022	0.715
0.17	0.142	1.626	1.138
0.28	0.141	1.585	1.109

3.1 Convergence studies

In this Section a convergence analysis of Ritz method is made to evaluate the differences between the use of GS orthogonal and non-orthogonal polynomials. For this purpose, two rectangular ($b = 3a$) plates are considered: a cross-ply orthotropic (L1) plate and a non-symmetric three-layers orthotropic sandwich plate (L2). The plate is simply supported on all edges under bi-sinusoidal load pressure. The numerical solution here obtained is compared with the exact and analytical trigonometric results computed by Iurlaro [95]. In the remainder of the paper, N_1 and N_2 are the numbers of GS orthogonal polynomials used in the Ritz method in x_1 and x_2 directions, respectively. The number p is the maximum number of the complete polynomials set used in the p-Ritz method.

Table 7 shows the results of Ritz method using GS orthogonal and non-orthogonal polynomials. Comparing the results obtained using 8 orthogonal polynomials or a complete set of functions with maximum degree 7, it is concluded that both sets of the admissible functions have the same convergence rate to the analytical results for the maximum displacement.

Differences between the two set of admissible functions appear when the free vibration problem is considered. Table 8 gives the first four non-dimensional circular frequencies for a simply supported square orthotropic sandwich plate (L3), with core-to-face thickness ratio and span-to-thickness ratio 10.

20

Table 7. Convergence of normalized maximum deflection $\bar{u}_3 = \frac{100 D_{11}}{q_0 a^4} u_3(0,0)$ for rectangular laminates (L1) and (L2) simply supported under bi-sinusoidal transverse load.

Non-orthogonal Polynomials (p-Ritz Method)			GS Orthogonal Polynomials (GS-Ritz Method)		
	L1	L2		L1	L2
p	$\bar{u}_3$		$N_1 = N_2$	$\bar{u}_3$	
1	1.9703	29.6618	1	0.2019	0.9171
2	1.9855	29.7279	2	1.9708	29.6650
3	2.4961	36.5167	3	1.9915	29.7503
4	2.4968	36.5194	4	2.5018	36.6693
5	2.5127	36.7814	5	2.5023	36.6708
6	2.5127	36.7816	6	2.5115	36.7869
7	2.5131	36.7876	7	2.5115	36.7869
8	2.5131	36.7876	8	2.5116	36.7882
9	2.5131	36.7878	9	2.5116	36.7882
10	2.5131	36.7878	10	2.5116	36.7882
3D Exact [95]	2.546	37.037	3D Exact [95]	2.546	37.037
			RZT [95]	2.512	36.788

Table 8. Comparison of convergence of first four non-dimensional circular $\left(\bar{\omega} = \omega \sqrt{\frac{a^4 \rho_f}{h E_{2_f}}} \right)$ between p-Ritz Method and Gram-Schmidt-Rayleigh-Ritz Method for laminate (L3).

Non-orthogonal Polynomials (p-Ritz Method)					GS Orthogonal Polynomials (GS-Ritz Method)				
p	$\bar{\omega}_{11}$	$\bar{\omega}_{12}$	$\bar{\omega}_{22}$	$\bar{\omega}_{13}$	$N_1 = N_2$	$\bar{\omega}_{11}$	$\bar{\omega}_{12}$	$\bar{\omega}_{22}$	$\bar{\omega}_{13}$
2	1.8823	3.50458	-	-	2	1.88143	-	-	-
3	1.85238	3.50178	4.72998	-	3	1.88137	3.49961	4.71693	-
4	1.85231	3.23587	4.72833	-	4	1.85165	3.49058	4.71603	-
5	1.85216	3.23578	4.32602	5.29058	5	1.85165	3.23317	4.31157	-
6	1.85214	3.23129	4.32549	5.29045	6	1.85158	3.23315	4.31157	5.28532
7	1.85214	3.23124	4.31268	5.24460	7	1.85158	3.22925	4.30540	5.28529
8	1.85212	3.23118	4.31239	5.24455	8	1.85158	3.22925	4.30540	5.24127
9	1.85211	3.23115	4.31203	5.24384	9	1.85158	3.22923	4.30537	5.24127
10	1.85211	3.23114	4.31189	5.24380	10	1.85158	3.22923	4.30537	5.24068
Iurlaro et al. [90]	$\bar{\omega}_{11}$		$\bar{\omega}_{12}$		$\bar{\omega}_{22}$		$\bar{\omega}_{13}$		
	1.852		3.229		4.305		5.241		

Table 8 shows how using GS orthogonal polynomials guarantees the convergence, with few terms ($N_1 = N_2 = 8$), of the first four frequencies to those analytically computed using trigonometric solution. Using non-orthogonal polynomials, it is necessary to increase the maximum degree p to have the convergence also for highest modes. It is concluded that at least for free vibration and dynamic response analysis, the GS orthogonal polynomials are preferable

in Ritz method. In the sequel of the paper, if not otherwise specified, eight GS orthogonal polynomials have been used in the x_1 and x_2 directions. The acronym TSDT is used to indicate numerical results obtained using Reddy TSDT [47].

3.2 Static Analysis

In this Section, different FG-CNTRC sandwich plates under mechanical loads and with different boundary conditions are analyzed. For bending problem, a simply supported square sandwich plate (L4a) with homogeneous core and FG-CNTRs face-sheet is considered (Figure 4 - Type A). The effects of plate side-to-thickness ratio, core-to-face-sheet thickness ratio, CNTs volume fraction, grading law and boundary conditions are analyzed. The core is made of Titanium alloy (Ti-6Al-4V) (see Table 4) and the face-sheets of PMMA/CNT composite (see Table 3). The grading law for lower and upper face-sheets are, respectively, FG-Λ and FG-V (see, Table 1). The non-dimensional quantities in this paper, if not otherwise specified, are defined as follows (E_{2_c} is the Young modulus of core):

$$\bar{u}_1 = \frac{h^2 E_{2_c} u_1}{q_0 a^3}; \quad \bar{u}_3 = \frac{h^3 E_{2_c} u_3}{q_0 a^4}; \quad \bar{\sigma}_{11} = \frac{h^2 \sigma_{11}}{q_0 a^2}; \quad \bar{\tau}_{13} = \frac{h \tau_{13}}{q_0 a} \tag{56}$$

Table 9. Bending of simply supported square sandwich plate (L4a) with FG-ΛV face-sheets. Effect of volume fraction of CNTs, h_c/h_f and a/h.

h_c/h_f	V_{cnt}^*	a/h	$\bar{u}_1\left(-\frac{a}{2},0,-\frac{h}{2}\right)$		$\bar{u}_3(0,0)$		$\bar{\sigma}_{11}\left(0,0,\frac{h}{2}\right)$		$\bar{\tau}_{13}\left(-\frac{a}{2},0,0\right)$	
			HSDT [51]	Present (eRZT)	HSDT [51]	Present (eRZT)	HSDT [51]	Present (eRZT)	HSDT [51]	Present (eRZT)
2	0.17	5	0.5463	0.5260	0.1036	0.1082	0.4476	0.4366	0.4021	0.4050
		10	0.8132	0.8054	0.0738	0.0751	0.6717	0.6613	0.3906	0.3939
6		5	0.5275	0.5218	0.0533	0.0552	0.4247	0.4287	0.3154	0.3177
		10	0.6535	0.6499	0.0470	0.0476	0.5383	0.5325	0.3183	0.3202
2	0.28	5	0.3603	0.3454	0.0906	0.0972	0.4809	0.4683	0.3970	0.4017
		10	0.5584	0.5517	0.0574	0.0597	0.7496	0.7377	0.3846	0.3887
6		5	0.4118	0.3998	0.0481	0.0505	0.5378	0.5351	0.3167	0.3191
		10	0.5375	0.5308	0.0404	0.0412	0.7190	0.7078	0.3205	0.3226

In Table 9, the eRZT results are compared with those computed by Natarajan et al [51] using the finite element method based on High Order structural Theory with 13 degrees of freedom. It is evident the ability of eRZT to provide very accurate results. Taking into account that the kinematics eRZT involves only 7 unknown kinematic variables, eRZT appears to be very effective from an accuracy/computational cost point of view.

Now, a square simply supported and fully clamped sandwich plate with functionally graded face-sheets (L5a) under bi-sinusoidal load with various span to thickness ratios is considered. In this case the core-to-face thickness ratio (h_c/h_f) is set to 4, and the volume fraction of CNTs for FG face-sheets to $V_{cnt}^* = 0.17$ (PMMA/CNT); the core's material is

Titanium alloy (Material T, Table 6). Table 10 shows the non-dimensional maximum central deflection. The results of eRZT for different topology of FG face-sheets are compared with those of CPT.

Table 10. Non-dimensional maximum deflection $\bar{u}_3 = 100 \frac{h^3 E_{2c} u_3}{q_0 a^4}$ for simply supported (SSSS) and fully clamped (CCCC) sandwich square plate (L5a) with different type of FG face-sheets ($V_{cnt}^* = 0.17$), under bi-sinusoidal load for various span-to-thickness ratios. In brackets the number of GS orthogonal polynomials used.

	SSSS ($N_1 = N_2 = 8$)							CCCC ($N_1 = N_2 = 9$)						
a/h	U-U	V-V	Λ-Λ	◊-◊	X-X	Λ-V	V-Λ	U-U	V-V	Λ-Λ	◊-◊	X-X	Λ-V	V-Λ
6	6.2920	6.2882	6.2882	6.2885	6.2880	6.3171	6.3503	2.5982	2.5969	2.5969	2.6086	2.5857	2.7430	2.4903
8	5.8943	5.8917	5.8917	5.8940	5.8878	5.8140	6.0419	2.2079	2.2066	2.2066	2.2103	2.2034	2.2967	2.1581
10	5.7016	5.6997	5.6997	5.7042	5.6924	5.5613	5.8971	2.0030	2.0019	2.0019	2.0034	2.0008	2.0484	1.9946
20	5.4347	5.4340	5.4340	5.4430	5.4198	5.2000	5.7018	1.6898	1.6896	1.6896	1.6915	1.6866	1.6405	1.7626
50	5.3577	5.3575	5.3575	5.3680	5.3407	5.0931	5.6467	1.5889	1.5893	1.5893	1.5928	1.5836	1.4989	1.6935
100	5.3466	5.3464	5.3464	5.3572	5.3293	5.0777	5.6388	1.5737	1.5741	1.5741	1.5780	1.5679	1.4769	1.6835
CPT	5.3429	5.3427	5.3427	5.3536	5.3255	5.0725	5.6361	1.5685	1.5690	1.5690	1.5731	1.5626	1.4694	1.6801

As expected, under the same mechanical load, the maximum central deflection for fully clamped case is lower than for simply supported case. For thin and relatively thick plates the FG-CNTs topology with the highest flexural rigidity is FG Λ-V type (for both simply supported and fully clamped cases). Considering very thick plates (*a/h*=6) the effect of boundary conditions on the maximum deflection is greater than the effect of the grading law of CNTs. In fact, for this particular case, the previous type of FG sandwich plate (Λ-V) has higher deformability than the typical FG plate (V-Λ) with the lower bending stiffness. Also, the eRZT results converge to CPT solution for thin sandwich plates.
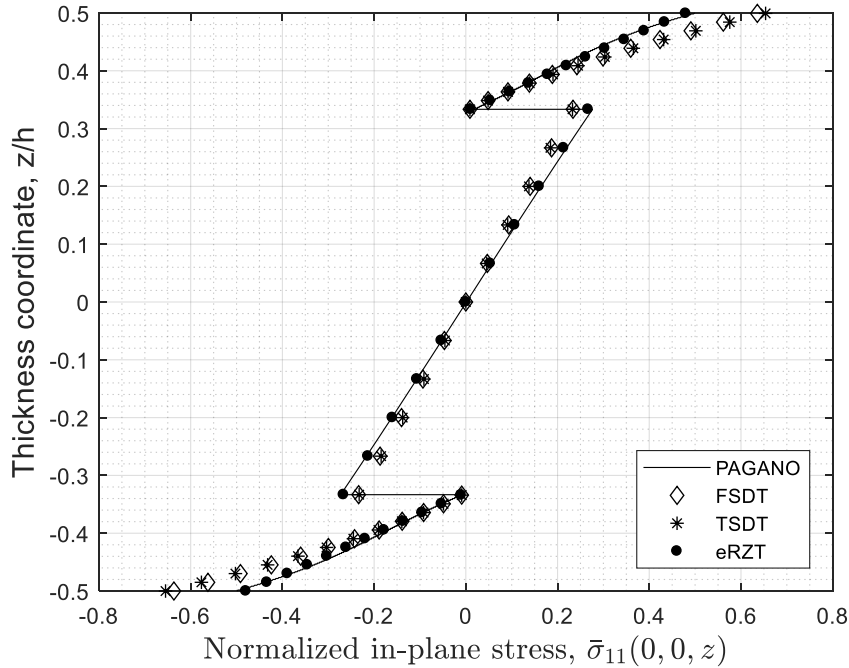
Figure 5. Non-dimensional in-plane stresses for simply supported sandwich square plate (L5a) with FG Λ-V under bi-sinusoidal load (*a/h*= 6). The volume fraction is $V_{cnt}^* = 0.17$.
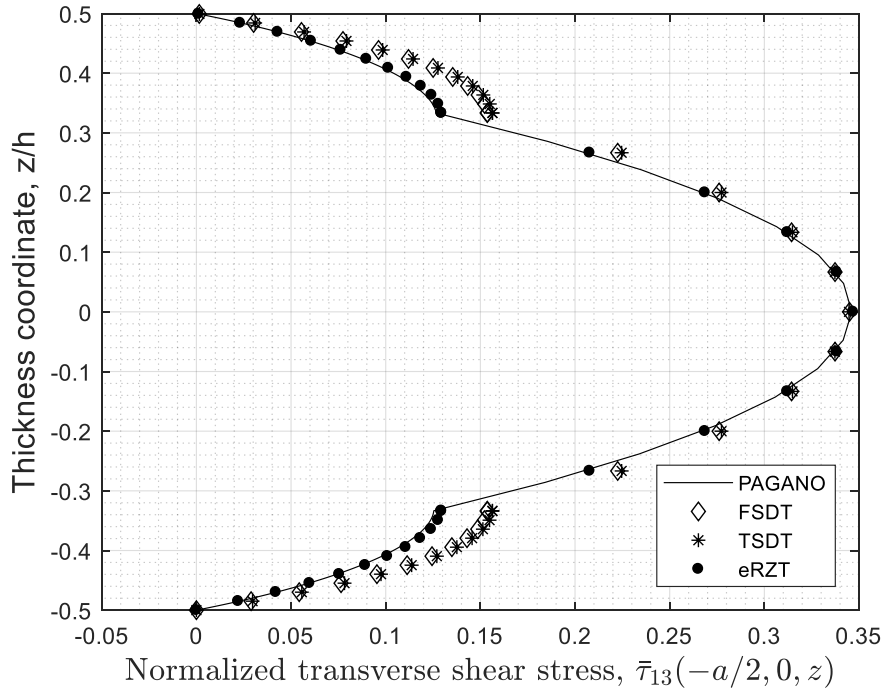
Figure 6. Non-dimensional shear stresses for simply supported sandwich square plate (L5a) with FG Λ-V under bi-sinusoidal load (a/h= 6). The volume fraction is $V_{cnt}^* = 0.17$.

For a simply supported square sandwich plate (L5a) with FG-ΛV face-sheets under bi-sinusoidal mechanical load, in Figures 5 and 6, the through the thickness in-plane and transverse shear stresses distributions are plotted. It is evident how the eRZT distributions are very close to the 3D exact solution obtained with Pagano method [103], while other theories, the FSDT ($k_1^2 = k_2^2 = 1$) and Reddy's TSDT are not capable to predict the stresses near layer interfaces. Another case considered is a cantilever (CFFF) rectangular sandwich plate (L5a) with FG face-sheets subjected to a constant transverse load of intensity q_0.

Table 11. Cantilevered rectangular plate (L5a) under transverse uniform load: normalized maximum deflection $\bar{u}_3 = 100 \frac{h^3 E_{2c} u_3}{q_0 a^4}$. $a/b = 4$, $h_c/h_f = 4$ ($N_1 = 10$, $N_2 = 8$).

$b/h = 4$	UD-UD	FG V-V	FG Λ-Λ	FG ◇-◇	FG X-X	FG Λ-V	FG V-Λ
$V_{cnt}^* = 0.12$	162.2125	162.3402	162.3402	162.8450	161.5884	150.3966	176.6046
$V_{cnt}^* = 0.17$	124.0508	124.1929	124.1929	124.6001	123.5083	113.9373	136.6281
$V_{cnt}^* = 0.28$	85.0426	85.1784	85.1784	85.4433	84.6487	77.8389	94.4271

Table 11 shows the maximum tip deflection for different FG face-sheet topologies and volume fraction of CNTs. It is evident that the FG Λ-V topology has the highest bending stiffness, while the most deformable plate has the FG V-Λ one. The differences between other topologies are not so evident. From Table 11, the effect of higher volume fractions of CNTs of FG face-sheets is highlighted. High volume fraction of CNTs in polymeric matrix significantly increases the plate stiffness and consequently decreases the deflection.

As a further example, a rectangular ($b = 2a$) simply supported sandwich plate (L6a) with FG-CNTRC core (PmPV/CNT) and piezoelectric isotropic (PZT-4) (see Table 3) face-sheets (Figure 4 - Type B) under bi-sinusoidal pressure is considered. The maximum central deflection as computed using eRZT is compared in Table 12 with 3D exact solution computed using Pagano method [103], for different topologies of FG (FG-U, FG-V, FG-Λ, FG-$\diamond$ and FG-X) and CNTs volume fractions. The span-to-thickness ratio is *a/h=10*.

Table 12. Simply-supported rectangular ($b=2a$, $a/h = 10$) sandwich plate (L6a) with FG core under bi-sinusoidal load of intensity q_0: normalized maximum central deflection $\bar{u}_3 = 100 \frac{h^3 E_{2_f} u_3}{q_0 a^4}$

V_{cnt}^*	**FG-U**		**FG-Λ**		**FG-V**		**FG-$\diamond$**		**FG-X**	
	3D	eRZT	3D	eRZT	3D	eRZT	3D	eRZT	3D	eRZT
0.11	17.6211	17.3821	18.3281	18.0800	18.3281	18.0800	19.0597	18.7990	16.7678	16.5480
0.14	16.6773	16.3689	17.4326	17.0851	17.4326	17.0851	18.1578	17.7805	15.8764	15.6255
0.17	13.1120	12.8388	13.9858	13.6624	13.9858	13.6624	14.8003	14.4527	12.2198	12.0128

As expected, for all types of functionally graded sandwich plates, increasing the volume fraction of CNTs, the maximum deflection decreases, because more CNTs phase increases mechanical characteristics, as said by the extended rule of mixture, and, consequently the bending stiffness. The stiffest sandwich plate is obtained using FG-X type, then FG-U, FG-Λ (or FG-V) and FG-$\diamond$, with the lowest bending rigidity. To exploit the great capability of the Ritz method for different boundary conditions, rectangular CCCC, CFCF and SSSS sandwich plates (L6a) with functionally FGCNTs core and piezoelectric face-sheet under uniform pressure are analyzed.

Table 13. Normalized maximum central deflection $\bar{u}_3 = 100 \frac{h^3 E_{2_f} u_3}{q_0 a^4}$ of sandwich rectangular plate (L6a) with FG core $a/h = 10$ under uniform pressure of intensity q_0. In brackets the number of GS polynomials used.

CCCC ($N_1 = N_2 = 10$)					
V_{cnt}^*	**FG-U**	**FG-Λ**	**FG-V**	**FG-$\diamond$**	**FG-X**
0.11	14.9418	14.9788	14.9788	15.1636	14.8046
0.14	14.3150	14.2311	14.2311	14.3971	14.2250
0.17	10.3702	10.3294	10.3294	10.4878	10.2835

CFCF ($N_1 = 10, N_2 = 8$)					
V_{cnt}^*	**FG-U**	**FG-Λ**	**FG-V**	**FG-$\diamond$**	**FG-X**
0.11	15.1950	15.2543	15.2543	15.4715	15.0325
0.14	14.5065	14.4326	14.4326	14.6222	14.4036
0.17	10.3458	10.3213	10.3213	10.4996	10.2479

SSSS ($N_1 = N_2 = 8$)					
V_{cnt}^*	**FG-U**	**FG-Λ**	**FG-V**	**FG-$\diamond$**	**FG-X**
0.11	25.4389	26.5670	26.5670	27.7272	24.0920
0.14	23.8801	25.0428	25.0428	26.1664	22.6766
0.17	18.7567	20.0873	20.0873	21.3597	17.4257

As expected, the results collected in Table 13 show that the values of deflection are influenced by the boundary conditions (a fully clamped rectangular sandwich rectangular sandwich plate is stiffer than the same plate with two opposite edge clamped and other two free or with four edges simply supported).

From the results of Table 12 and 13 it is concluded that the best way to arrange the CNTs to get a stiffer plate (moderately thick) is FG-X; using FG-Λ or FG-V give the same stiffness; the most flexible sandwich plate is that with FG-◊ core.

3.3 Buckling Analysis

In this section the buckling problem of sandwich plates with CNTs reinforced face-sheet or core is considered. A comparison is made with the results of Shen et al [104]. A simply supported square sandwich plate (L4b) with different CNTs volume fraction for face-sheets and core-to-face thickness ratios under uni-axial compression in x_1-direction (P_{11}) is considered. The homogeneous core is made of Titanium alloy (Material T) (see Table 4), while the matrix for the face-sheet is made of PMMA/CNT (see Table 3).

Table 14. Comparison of critical uni-axial buckling loads (P_{11cr} in kN) obtained with different theories for a simply supported square sandwich plate with FG face sheet (L4b) ($a/h=20$).

$h_c/h_f = 8$ $(h = 10\ mm)$	V_{cnt}^*	CPT	FSDT $k_1^2 = k_2^2 = 1$	FSDT $k_1^2 = ad\ hoc^\bullet$ $k_2^2 = ad\ hoc^\bullet$	TSDT [104]	TSDT	eRZT
FG Λ-V	0.12	1192.96	1181.96	1170.37	1181.28	1181.12	1179.47
	0.17	1297.89	1284.65	1273.19	1284.26	1284.03	1281.56
	0.28	1488.55	1470.35	1449.53	1470.06	1470.37	1462.19
$h_c/h_f = 6$ $(h = 8\ mm)$	V_{cnt}^*	CPT	FSDT $k_1^2 = k_2^2 = 1$	FSDT $k_1^2 = ad\ hoc^\bullet$ $k_2^2 = ad\ hoc^\bullet$	TSDT [104]	TSDT	eRZT
FG Λ-V	0.12	683.08	676.95	665.96	676.96	676.751	673.81
	0.17	764.07	756.19	745.29	756.51	756.24	752.26
	0.28	911.48	899.54	879.35	900.08	900.255	889.43
$h_c/h_f = 4$ $(h = 6\ mm)$	V_{cnt}^*	CPT	FSDT $k_1^2 = k_2^2 = 1$	FSDT $k_1^2 = ad\ hoc^\bullet$ $k_2^2 = ad\ hoc^\bullet$	TSDT [104]	TSDT	eRZT
FG Λ-V	0.12	322.86	319.96	310.27	320.33	320.12	315.87
	0.17	380.04	375.85	365.95	376.56	376.27	370.72
	0.28	484.44	477.03	457.78	478.09	478.14	464.17

$^\bullet$ Shear correction factors [105]: for $h_c/h_f = 8$: $k_1^2 = 0.4997$ and $k_2^2 = 0.4508$ ($V_{cnt}^* = 0.12$), $k_1^2 = 0.5471$ and $k_2^2 = 0.4951$ ($V_{cnt}^* = 0.17$), $k_1^2 = 0.4715$ and $k_2^2 = 0.4199$ ($V_{cnt}^* = 0.28$); for $h_c/h_f = 6$: $k_1^2 = 0.3664$ and $k_2^2 = 0.3215$ ($V_{cnt}^* = 0.12$), $k_1^2 = 0.4263$ and $k_2^2 = 0.3759$ ($V_{cnt}^* = 0.17$), $k_1^2 = 0.3712$ and $k_2^2 = 0.3238$ ($V_{cnt}^* = 0.28$); for $h_c/h_f = 4$: $k_1^2 = 0.2304$ and $k_2^2 = 0.1969$ ($V_{cnt}^* = 0.12$), $k_1^2 = 0.2960$ and $k_2^2 = 0.2542$ ($V_{cnt}^* = 0.17$), $k_1^2 = 0.2697$ and $k_2^2 = 0.2305$ ($V_{cnt}^* = 0.28$).

In Table 14 the values of the buckling load are collected. The thickness ratio is assumed to be constant for all values of core-to-face thickness ratios and is equal to $a/h = 20$. As expected, the CPT is stiffer than the other theories, in fact from Table 14, CPT overestimates critical buckling loads. FSDT takes into consideration the effect of shear deformability and the values for uni-axial buckling load decrease. Using an appropriate shear correction factor for

FSDT evaluated following Raman et al formulation [105] based on energetic consideration, the buckling loads are under-estimated with respect to those computed with eRZT. The TSDT [47] results are very close with FSDT (without any shear correction factor) and with those presented in the literature [104]. It is evident from Table 14 that increasing the distance between face-sheet increases the uni-axial buckling loads.

In the next example, rectangular and square sandwich plates (L5b) with different FG face-sheets under bi-axial compression load ($r_{11} = 0.5, r_{12} = 0$, see Eq. (52)) are analyzed. Three boundary conditions are considered: fully clamped (CCCC), two opposite sides clamped and the others simply supported (CSCS) and fully simply supported (SSSS). The core-to-face thickness ratio is assumed to be equal $h_c/h_f = 6$ and the span-to-thickness ratio is 5 (thick plates). The volume fraction of carbon nanotube is $V^*_{cnt} = 0.28$. The core material is Titanium alloy (Material T, see Table 4) and the face-sheets are made of PMMA/CNT (see Table 3). If not otherwise stated, the results in Table 15 refer to the critical bi-axial load parameters for first buckling mode (with one half-wave both in x_1 and x_2 directions). For all FG topologies and plates geometry, the bi-axial buckling load parameters increase from simply supported to fully clamped case. When all sides of plates are clamped the values of parameters are the highest. As shown in Table 15, the effect of the aspect ratio of sandwich plate is relevant, rectangular plate $b = 0.5a$ has higher values than the $b = 2a$ case. The combination of boundary condition and aspect ratio geometry could increase the parameters and, in particular for CCCC case with $b = 0.5a$, the buckling load parameters correspond to a buckling mode with two half-wawes in the x_1 direction. In contrast to the uni-axial compressive case, the effect of bi-axial compressive load combined with the various types of FG give a buckling parameter higher for FG V-Λ than FG Λ-V.

Table 15. Comparison of bi-axial buckling load parameters $\lambda = P^{cr}_{11}a^2/(E_{2_c}h^3)$ for rectangular and square sandwich plate (L5b) with different FG face-sheet (see Figure 4, Type B). For CCCC and CSCS, $N_1 = N_2 = 10$. The core-to-face thickness ratio is $h_c/h_f = 6$ and $V^*_{cnt} = 0.28$ (a/h=5).

| $b = 2a$	UD-UD	V-V	Λ-Λ	◊-◊	X-X	Λ-V	V-Λ
CCCC	2.5004	2.5034	2.50343	2.4724	2.5040	2.2322	2.7275
CSCS	2.4797	2.4824	2.4824	2.4496	2.5119	2.1969	2.7246
SSSS	1.1017	1.1025	1.1025	1.1020	1.1027	1.0531	1.1209
$b = a$	UD-UD	V-V	Λ-Λ	◊-◊	X-X	Λ-V	V-Λ
CCCC	2.9248	2.9300	2.9300	2.9071	2.9498	2.7322	3.0938
CSCS	2.3962	2.3994	2.3994	2.3750	2.4211	2.1907	2.5753
SSSS	1.3698	1.3719	1.3719	1.3715	1.3720	1.3381	1.3832
$b = 0.5a$	UD-UD	V-V	Λ-Λ	◊-◊	X-X	Λ-V	V-Λ
CCCC	5.1328[b]	5.1413[b]	5.1413[b]	5.0782[b]	5.1905[b]	4.8822[b]	5.3670[b]
CSCS	3.2011	3.2082	3.2082	3.1976	3.2168	3.1240	3.2762
SSSS	2.7888	2.7957	2.7957	2.7954	2.7958	2.7865	2.7947

[b]Buckling mode (2,1)

The same previous rectangular sandwich plate (L5b) is analyzed with in-plane shear load P_{12}. Also, in this example, three types of boundary conditions are considered: fully clamped (CCCC), two opposite side clamped and the others two simply supported (CSCS), fully simply supported (SSSS).

Table 16. Comparison of in-plane shear buckling load parameters $\lambda = P_{12}^{cr} a^2 / (E_{2_c} h^3)$ for rectangular and square sandwich plate (L5b) with different FG face-sheet. ($N_1 = N_2 = 10$). The core-to-face thickness ratio is $h_c/h_f = 6$ and $V_{cnt}^* = 0.28$ (a/h=5).

$b = 2a$	UD-UD	V-V	Λ-Λ	◊-◊	X-X	Λ-V	V-Λ
CCCC	3.4635[c]	3.4688[c]	3.4688[c]	3.4343[c]	3.4971[c]	3.2771[b]	3.6166[c]
CSCS	3.4034[c]	3.4084[c]	3.4084[c]	3.3735[c]	3.4373[c]	3.2244[c]	3.5621[c]
SSSS	2.8970[b]	2.9011[b]	2.9011[b]	2.8827[b]	2.9172[b]	2.7471[b]	3.0175[b]
$b = a$	UD-UD	V-V	Λ-Λ	◊-◊	X-X	Λ-V	V-Λ
CCCC	4.0934	4.1000	4.1000	4.0665	4.1277	3.9292	4.2423
CSCS	3.9169	3.9227	3.9227	3.8869	3.9524	3.7312	4.0816
SSSS	3.4075	3.4130	3.4130	3.3971	3.4262	3.2873	3.5061
$b = 0.5a$	UD-UD	V-V	Λ-Λ	◊-◊	X-X	Λ-V	V-Λ
CCCC	5.9887[b]	5.9976[b]	5.9976[b]	5.9612[b]	6.0246[b]	5.8727[b]	6.1014[b]
CSCS	5.6469[b]	5.6553[b]	5.6553[b]	5.6214[b]	5.6821[b]	5.5226[b]	5.7674[b]
SSSS	5.5629[b]	5.5780[b]	5.5780[b]	5.5517[b]	5.5983[b]	5.4553[b]	5.6789[b]

[b] Second mode shear buckling; [c] Third mode shear buckling
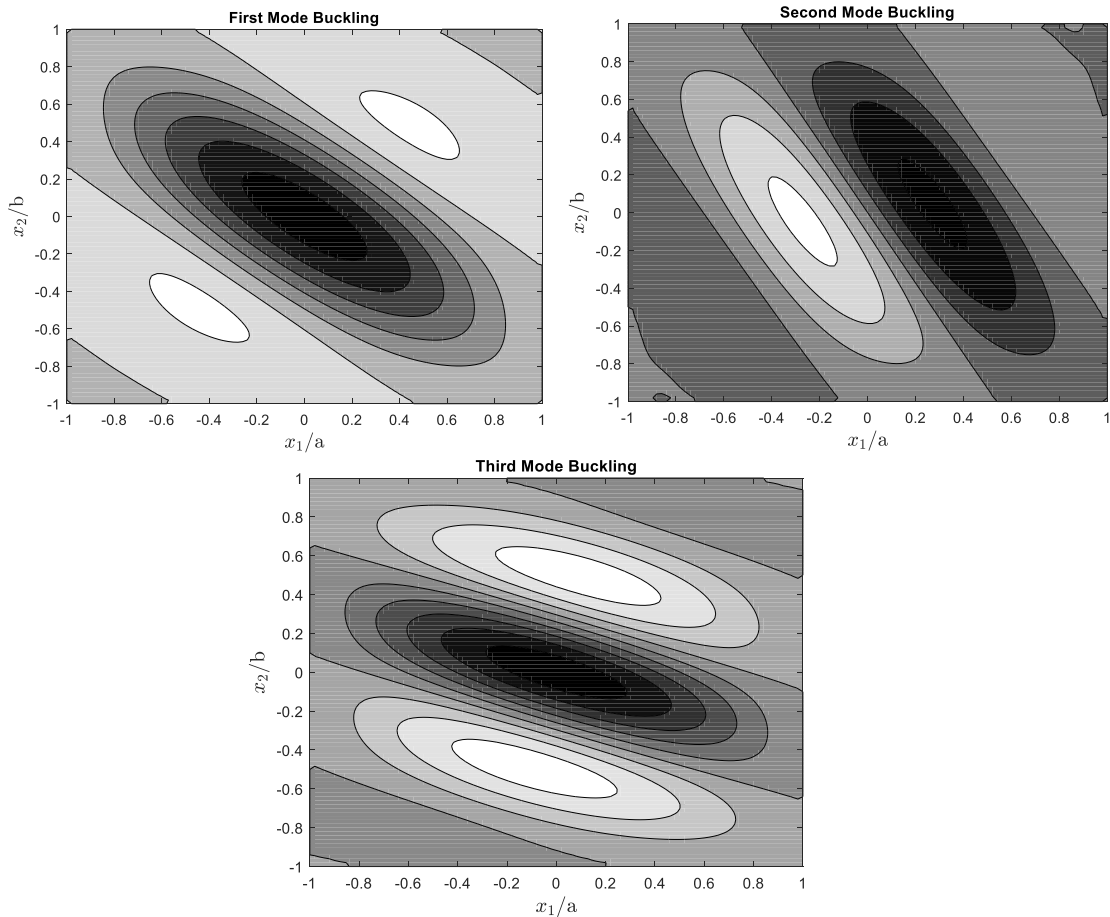
Figure 7. Shear buckling shapes for CCCC FG-VΛ (L5b) sandwich plate: First Mode Buckling ($b = a$), Second Mode Buckling ($b = 0.5a$), Third Mode Buckling ($b = 2a$)

The results are collected in Table 16. It is observed that the effect of combination of aspect ratio and FG topology is similar to that observed for bi-axial compressive load problem. The highest values are obtained for FG V-Λ type sandwich and the lowest ones for FG Λ-V type sandwich. For rectangular plate, the combination of FG for face-sheet, geometry and especially boundary condition, leads to having a buckling parameter that corresponds to a buckling mode with two or three half-waves along the diagonal direction. As expected, the critical buckling parameters increase with more restrained edges.

Wu et al [80] studied the stability of carbon nanotubes reinforced composite plates with surface-bonded piezoelectric layers using the finite layer method. To assess the capability of present formulation to predict the critical buckling loads also for this type of sandwich plate with functionally graded core (L6b), the results obtained by Wu et al [80] are compared with present eRZT. Different span-to-thickness ratios, CNTs volume fractions and topologies of FG for core are considered. The material for face-sheet as indicated by Wu et al [80] is PZT-5A, while the composite core is made of PmPV reinforced by SWCNTs (10,10) (see Table 3). Two types of compressive loads are considered: uni-axial in x_1 direction and bi-axial of equal intensity for both x_1 and x_2 directions. The authors [80] considered also a pre-buckling state with an initial membrane traction stress-state for piezoelectric layers but in this example, they are not taken in consideration, so it is expected that the critical buckling parameters obtained are lower. Because there are few differences between the two cases of piezoelectric conditions (open/close circuit) in reference work [80], here are compared those coming from open circuit case.

Table 17. Critical buckling load parameters $\lambda = P_{11}^{cr} b^2 / (E_m h^3)$ for square sandwich (L6b), with PZT-5A material for face-sheet and FG-CNTR for core, under uni-axial compressive loads. E_m is the Young's modulus of matrix (PmPv).

V_{cnt}^*	a/h (m,n)	Wu et al [80]			eRZT		
		FG-U	FG-◊	FG-X	FG-U	FG-◊	FG-X
0.11	5 (3,1)	11.1528	10.9999	11.2257	10.9105	10.8611	11.2179
	10 (2,1)	35.4755	35.0496	35.6151	34.6314	34.2706	34.7250
	50 (1,1)	80.7073	72.4404	88.7498	70.4541	62.0209	78.6703
0.14	5 (3,1)	11.5628	11.4068	11.6831	11.3048	11.3775	11.8026
	10 (2,1)	36.847	36.4906	36.9270	36.1578	36.1266	36.0475
	50 (1,1)	85.47522	74.9529	95.6359	75.2896	64.5532	85.6711
0.17	5 (3,1)	16.5336	16.5044	16.6461	16.1144	16.8052	16.6702
	10 (1,1)	50.2861	47.8790	50.9401[b]	47.0374	44.2047	48.7561
	50 (1,1)	92.0902	78.9165	104.9243	81.6589	68.2684	94.7169

[b] Second mode buckling (2,1)

Results presented in Table 17 are very close to those computed by Wu et al [80] for thick and relatively thick sandwich plates ($a/h = 5, 10$). For thin plate (a/h=50), as indicated by the authors [80], the effect of pre-stresses is more evident for critical buckling load parameters. As expected, the FG-X topology has the highest values for critical uni-axial buckling load.

Table 18. Critical buckling load parameters $\lambda = P_{11}^{cr} b^2 / (E_m h^3)$ for square sandwich (L6b), with PZT-5A material for face-sheet and FG CNTRC for core, under bi-axial compressive loads. E_m is the Young's modulus of matrix (PmPv).

V_{cnt}^*	a/h (m,n)	Wu et al [80]			eRZT		
		FG-U	FG-◊	FG-X	FG-U	FG-◊	FG-X
0.11	5 (1,1)	7.7162	7.7294	7.7035	7.4817	7.4969	7.4687
	10 (1,1)	19.3925	18.8658	19.7367	18.1373	17.4708	18.5733
	50 (1,1)	40.3390	36.2050	44.3615	35.227	31.0105	39.3351
0.14	5 (1,1)	7.9800	8.0083	7.9619	7.7450	7.7982	7.7167
	10 (1,1)	20.0855	19.4918	20.4374	18.8901	18.1548	19.3174
	50 (1,1)	42.7215	37.4602	47.8029	37.6448	32.2766	42.8356
0.17	5 (1,1)	10.9369	10.9593	10.9125	10.5932	10.6600	10.5425
	10 (1,1)	25.0509	23.8550	25.8010	23.5187	22.1023	24.3781
	50 (1,1)	46.0277	39.4412	52.4457	40.8294	34.1342	47.3584

Table 18 collects buckling load parameter results for bi-axial compressive load (r_{11}=1 and r_{12}=0 in Eq. (52)) for the same sandwich plate (L6b) of Table 17.

The eRZT results are very close to those of Ref. [80]. Also, in this case the effect of pre-stresses is more evident for thin sandwich plates than for thick ones. The combination of bi-axial compressive loads and FG type produces higher buckling loads for FG-◊ than for FG-X sandwich plates, contrary to what happens for the uni-axial compressive load cases.

3.4 Vibration Analysis

In this section, rectangular and square sandwich plates with functionally graded face-sheets (Type A, Figure 4) and core (Type B, Figure 4) are analyzed.

The results of Mohammadimehr et al [101] for a simply supported sandwich square plate (L7) FG-CNTs face-sheet are compared with those computed with eRZT and other theories (CPT, FSDT and TSDT). Different volume fractions and FG topologies are considered. The face-sheets are made of PMMA reinforced by (10,10) SWCNTs, the soft-core is made of Divinycell HD 100 with temperature dependent material's properties [101]. For this analysis the temperature considered is T=300 K.

Table 19. Comparison using different theories of the first two non-dimensional circular frequencies $\Omega = \frac{\omega b^2}{h_f}\sqrt{\frac{\rho_c}{E_{3c}}}$ for simply supported sandwich square plate (L7) ($b = 500\ mm, h = 35\ mm$) with various FG face-sheet.

h_c/h_f		UD-UD						
5				FSDT				
V_{cnt}^*	Mode Number	CPT	$k_1^2 = k_2^2 = 1$	$k_1^2 = k_2^2 = 5/6$	$k_1^2 = ad\ hoc^\bullet$ $k_2^2 = ad\ hoc^\bullet$	TSDT	[101]	eRZT
0.12	(1,1)	286.32	202.371	193.261	79.9214	124.576	83.882	83.7616
	(1,2)	355.18	276.398	267.834	132.429	196.651	135.639	135.564
0.17	(1,1)	345.94	252.426	241.757	85.7549	152.865	89.475	89.3491
	(1,2)	439.625	350.678	340.454	139.158	245.763	144.382	144.28
0.28	(1,1)	430.311	284.997	270.75	84.0228	162.563	93.055	92.8372
	(1,2)	514.26	380.455	367.431	139.218	257.987	146.767	146.606

h_c/h_f		X-X						
5				FSDT				
V_{cnt}^*	Mode Number	CPT	$k_1^2 = k_2^2 = 1$	$k_1^2 = k_2^2 = 5/6$	$k_1^2 = ad\ hoc^\bullet$ $k_2^2 = ad\ hoc^\bullet$	TSDT	[101]	eRZT
0.12	(1,1)	287.005	202.941	193.813	80.2781	126.306	85.972	85.7556
	(1,2)	356.315	277.401	268.815	133.034	198.462	137.159	137.015
0.17	(1,1)	346.914	253.709	243.038	84.1945	155.827	92.375	92.1569
	(1,2)	441.918	353.137	342.889	139.895	249.433	146.600	146.444
0.28	(1,1)	432.007	290.043	275.831	84.7397	169.725	97.698	97.3223
	(1,2)	520.350	389.279	376.222	140.364	268.115	150.765	150.527

h_c/h_f		◇-◇						
5				FSDT				
V_{cnt}^*	Mode Number	CPT	$k_1^2 = k_2^2 = 1$	$k_1^2 = k_2^2 = 5/6$	$k_1^2 = ad\ hoc^\bullet$ $k_2^2 = ad\ hoc^\bullet$	TSDT	[101]	eRZT
0.12	(1,1)	285.817	202.555	193.482	79.6855	123.409	81.875	81.8243
	(1,2)	355.305	277.089	268.546	132.097	196.082	134.446	134.395
0.17	(1,1)	345.47	253.185	242.583	83.5542	151.608	86.745	86.6765
	(1,2)	440.655	352.672	342.48	138.814	245.497	142.669	142.57
0.28	(1,1)	430.132	289.499	275.365	84.0687	162.424	88.962	88.8674
	(1,2)	518.527	388.638	375.646	139.23	260.639	144.201	144.086

h_c/h_f		V-V						
5				FSDT				
V_{cnt}^*	Mode Number	CPT	$k_1^2 = k_2^2 = 1$	$k_1^2 = k_2^2 = 5/6$	$k_1^2 = ad\ hoc^\bullet$ $k_2^2 = ad\ hoc^\bullet$	TSDT	[101]	eRZT
0.12	(1,1)	286.028	202.627	193.545	79.7938	124.456	82.625	82.5532
	(1,2)	355.517	277.175	268.623	132.271	197.051	135.017	134.954
0.17	(1,1)	345.727	253.285	242.671	83.6705	153.286	87.782	87.6961
	(1,2)	440.943	352.814	342.611	139.011	247.275	143.559	143.453
0.28	(1,1)	430.463	289.608	275.461	84.1916	165.686	90.584	90.454
	(1,2)	518.943	388.848	375.844	139.437	264.369	145.724	145.593

h_c/h_f		Λ-V						
5				FSDT				
V_{cnt}^*	Mode Number	CPT	$k_1^2 = k_2^2 = 1$	$k_1^2 = k_2^2 = 5/6$	$k_1^2 = ad\ hoc^\bullet$ $k_2^2 = ad\ hoc^\bullet$	TSDT	[101]	eRZT
0.12	(1,1)	300.342	207.1	197.37	83.3147	125.934	85.198	85.1006
	(1,2)	367.742	280.828	271.765	137.73	197.081	136.825	136.779
0.17	(1,1)	363.113	259.373	247.939	87.509	153.248	90.279	90.226
	(1,2)	456.216	358.267	347.405	145.4	245.279	145.690	145.656
0.28	(1,1)	453.026	295.888	280.826	88.2727	160.325	93.412	93.344
	(1,2)	540.963	396.364	382.587	146.254	257.065	149.090	149.053

h_c/h_f				V-Λ				
5				FSDT				
V_{cnt}^*	Mode Number	CPT	$k_1^2 = k_2^2 = 1$	$k_1^2 = k_2^2 = 5/6$	$k_1^2 = ad\ hoc^\blacklozenge$ $k_2^2 = ad\ hoc^\blacklozenge$	TSDT	[101]	eRZT
0.12	(1,1)	271.769	197.791	189.38	76.2472	122.639	80.134	80.0667
	(1,2)	343.48	273.302	265.279	126.676	196.743	133.277	133.185
0.17	(1,1)	328.407	246.736	236.966	79.7981	152.567	85.367	85.2319
	(1,2)	425.875	347.076	337.549	132.522	248.469	141.486	141.298
0.28	(1,1)	407.942	282.764	269.58	80.0899	168.979	87.817	87.6054
	(1,2)	497.061	380.918	368.727	132.567	268.811	142.401	142.156

$^\blacklozenge$Shear correction factors listed in Table 20

Table 20. Shear correction factors for Table 19 computed using Raman et al [105].

| V_{cnt}^*	UD-UD		X-X		◊-◊		V-V		Λ-V		V-Λ	
	k_1^2	k_2^2	k_1^2	k_2^2	k_1^2	k_2^2	k_1^2	k_2^2	k_1^2	k_2^2	k_1^2	k_2^2
0.12	0.06657	0.05587	0.06657	0.05587	0.06557	0.05503	0.06578	0.05521	0.07291	0.06117	0.05902	0.04954
0.17	0.04024	0.03367	0.04024	0.03367	0.03932	0.03291	0.03944	0.03301	0.04378	0.03663	0.03534	0.02958
0.28	0.03593	0.03006	0.03593	0.03006	0.03378	0.02825	0.03388	0.02834	0.03763	0.03147	0.03033	0.02537

When compared with the results of Ref. [101], all the theories used in Table 19, except eRZT, provide much higher frequency parameter, i.e., the plates are stiffer. Only FSDT with Raman's shear correction factor [105] under-estimates the values for the first two frequencies. Only eRZT produces results very close to those of Mohammadimehr et al [101], although the present formulation is simpler than Higher-Order Sandwich Plate Theory (HSAPT) used in [101]. From Table 19, it is clear how generally the FSDT and the TSDT might not be capable to predict the global response for a sandwich plate with soft-core material as well shown by Wang et al [28], Mohammadimehr et al [101], Yang et al [106], Frostig et al [107] and by Wu et al [108]. As expected, increasing the CNTs volume fraction the frequencies increase accordingly. Using FG X-X topology for face-sheet guarantee the highest flexural rigidity and values of frequencies. Two rectangular sandwich plates (L5a) with span-to-thickness ratio $a/h = 5$, core-to-face thickness ratio $h_c/h_f = 4$ with various FG topologies and boundary condition are analyzed. The material for core is Titanium alloy and the face-sheets are made of PMMA matrix reinforced by (10,10) SWCNTs (see, table 6). The volume fraction considered is $V_{cnt}^* = 0.17$. The following boundary conditions are considered: CCCC, SCSC, SFCS, CFSF and CFFF. For a better convergence of the results collected in Table 21, 10 GS orthogonal polynomials for both x_1 and x_2 directions were required.

Table 21. First five non-dimensional circular frequencies $\Omega = \frac{\omega a^2}{h}\sqrt{\frac{\rho_c}{E_{2c}}}$ for rectangular and square plate (L5a) with different boundary conditions and *a/h=5*. In brackets, the number of half-waves for the corresponding frequencies

BCs		Λ-V		X-X		◊-◊		V-Λ	
		$(a=b)$	$(a=3b)$	$(a=b)$	$(a=3b)$	$(a=b)$	$(a=3b)$	$(a=b)$	$(a=3b)$
CCCC	1	6.8351 (1,1)	23.4430 (1,1)	7.0639 (1,1)	23.4864 (1,1)	7.0076 (1,1)	23.4716 (1,1)	7.2107 (1,1)	23.5055 (1,1)
	2	11.6278 (1,2)	26.1277 (2,1)	11,7335 (1,2)	26.3808 (2,1)	11.7042 (1,2)	26.2729 (2,1)	11.7982 (1,2)	26.5099 (2,1)
	3	16.4188 (2,1)	30.7742 (3,1)	13.3362 (2,1)	31.3815 (3,1)	13.0767 (2,1)	31.091 (3,1)	13.6840 (2,1)	31.6625 (3,1)
	4	17.5240 (2,2)	36.9141 (4,1)	16.8357 (2,2)	37.9169 (4,1)	16.6654 (2,2)	37.3802 (4,1)	17.0598 (2,2)	38.3338 (4,1)
	5	18.3691 (1,3)	44.1722 (5,1)	18.4146 (1,3)	44.8115 (1,2)	18.398 (1,3)	44.7398 (5,1)	18.4358 (1,3)	44.9063 (1,2)
SCSC	1	5.5581 (1,1)	23.1298 (1,1)	5.5833 (1,1)	23.1191 (1,1)	5.5830 (1,1)	23.1174 (1,1)	5.5822 (1,1)	23.0962 (1,1)
	2	10.8871 (2,1)	25.408 (2,1)	11.0243 (1,2)	25.5748 (2,1)	11.0236 (1,2)	25.5414 (2,1)	11.0144 (1,2)	25.6794 (2,1)
	3	11.0210 (1,2)	29.7057 (3,1)	11.3908 (2,1)	30.3281 (3,1)	11.2882 (2,1)	30.0919 (3,1)	11.7277 (2,1)	30.6968 (3,1)
	4	15.2581 (2,2)	35.7659 (4,1)	15.5583 (2,2)	36.9245 (4,1)	15.4977 (2,2)	36.3462 (4,1)	15.7603 (2,2)	37.4736 (4,1)
	5	18.0598 (1,3)	43.1188 (5,1)	18.0507 (1,3)	44.7283 (5,1)	18.8914 (3,1)	43.8025 (5,1)	18.032 (1,3)	44.8158 (1,2)
SFCS	1	4.1965	5.0928	4.3849	5.2293	4.3572	5.2062	4.4983	5.3107
	2	5.9988	11.6025	6.1119	12.1582	6.0920	11.9866	6.1787	12.4943
	3	10.5128	19.1584	10.7399	20.2404	10.7289	19.7807	10.7611	20.8071
	4	10.6966	21.3352	11.2158	21.3326	11.0000	21.3279	11.6367	21.3223
	5	12.1834	25.2958	12.7021	25.3681	12.5414	25.3431	13.0163	25.4075
CFSF	1	4.0377	4.0185	4.2370	4.2195	4.2084	4.1908	4.3569	4.3404
	2	4.5793	6.6637	4.7437	6.7322	4.7181	6.7173	4.8425	6.7713
	3	7.1032	10.2636	7.18711	11.0055	7.17058	9.50066	7.23529	11.4482
	4	10.3274	13.8649	11.0568	14.156	10.8331	14.0661	11.4926	14.3345
	5	10.9554	17.821	11.5969	19.1624	11.3995	18.5887	11.9824	19.8521
CFFF	1	1.2226	1.216	1.2078	1.2018	1.2046	1.1987	1.1761	1.1700
	2	1.8277	3.2550	1.8344	3.2731	1.8306	3.2681	1.8271	3.2813
	3	4.8215	5.5535	4.8425	5.8137	4.8353	5.7575	4.8469	5.9575
	4	5.6242	9.9274	5.8730	10.0373	5.8174	10.0010	6.0113	10.0972
	5	6.4903	12.4545	6.7017	13.2881	6.6505	13.0249	6.8170	13.7583

Table 21 shows the effect of boundary conditions, aspect ratio and topologies of FG face-sheets on the natural frequencies. For a rectangular plate, all frequencies are higher than those of the corresponding square plate. Except for SCSC, the FG V-Λ sandwich topology shows the highest flexural rigidity followed by the FG X-X topology. Comparing these results with those obtained in Table 19, the effect of boundary conditions is very evident. FG X-X has always high frequencies, but for simply supported plate another stiff sandwich is FG Λ-V; for fully clamped plate, for example, the stiffer is FG V-Λ. This effect is shown also for SFCS, CFSF and CFFF. For SCSC the stiffer is FG Λ-V sandwich type as for simply supported case. For one or more clamped edges, with carbon nanotubes aligned along the

normal to these edges, there is an inversion of the stiffness between FG V-Λ and FG Λ-V sandwich types. In Figure 8 the five modal shapes of SFCS rectangular sandwich plate with FG X-X topology are plotted.
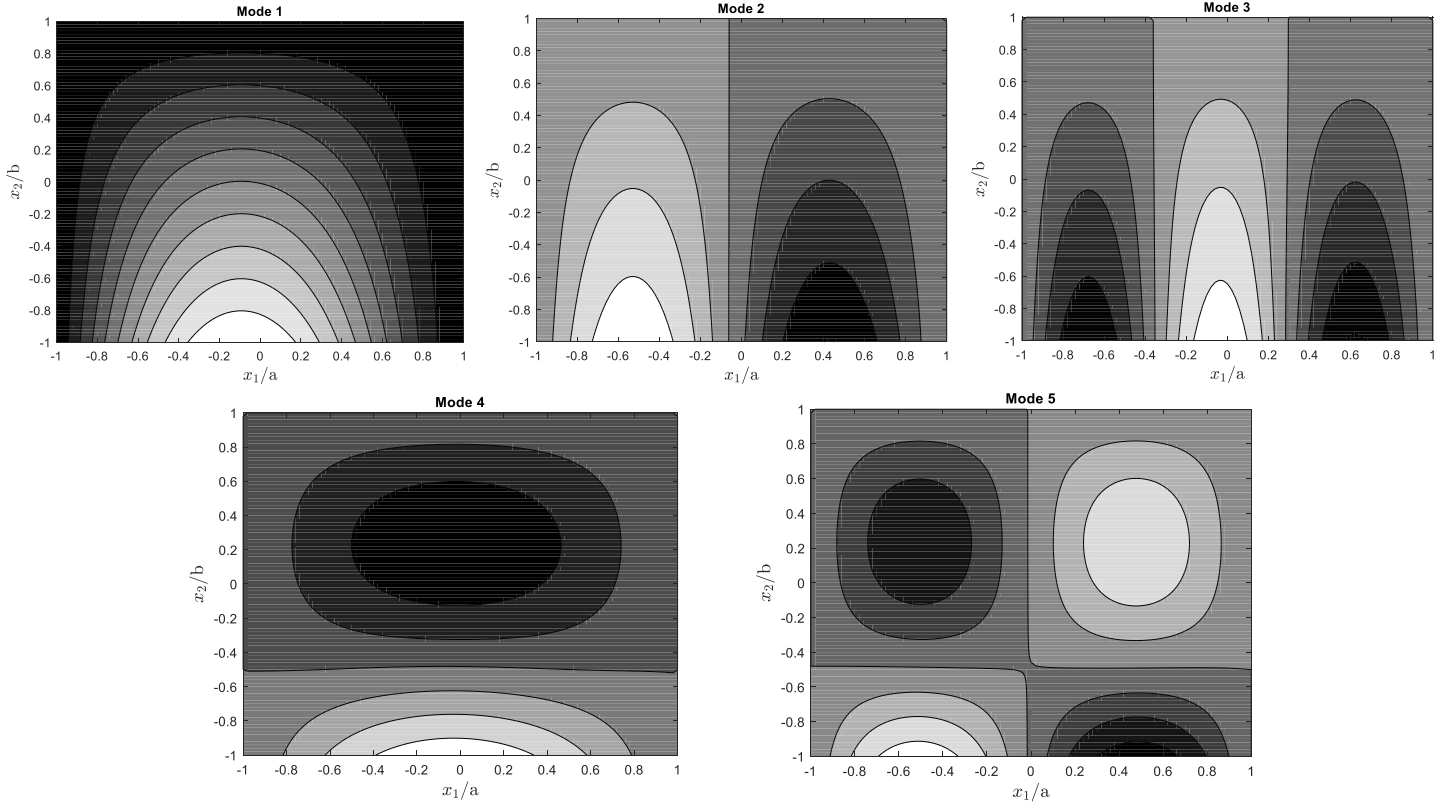
Figure 8. First five modal shapes of SFCS rectangular sandwich plate (L5a) with FG X-X face-sheets

Let us consider a simply supported square sandwich plate (L6a) of type B (see, Figure 4) with different topologies of FG core (FG-U, FG-◇ and FG-X) and PZT-4 material for face-sheet.

Table 22. Fundamental non-dimensional circular frequency $\Omega = 10\omega h \sqrt{\frac{\rho_f}{E_{1_f}}}$ for SSSS sandwich square plate (L6a) with FG-CNTRC core and PZT-4 face-sheet ($h_c/h_f = 8$) (*a/h=10*).

	Wu et al [102]	eRZT
FG-U	0.6621	0.6408
FG-O	0.6509	0.6267
FG-X	0.6690	0.6491

Table 22 compares the eRZT results with those taken from Wu et al [102] where the authors considered a piezoelectric pre-stress state of membrane traction and used the modified Pagano 3D theory. The volume fraction of CNTs is $V_{cnt}^* = 0.17$; the total thickness is $h = 1mm$ and the span-to-thickness ratio is 10. The material for core is PmPV with (10,10) SWCNTs as reinforcement. Because in the present analysis no effect of piezoelectric pre-stress state is taken into consideration, it is expected that the eRZT results are lower than those of Ref [102]. By taking into account this effect, it can be concluded that eRZT results match very well the 3D results. As for buckling case (see, Table 17 and Table 18), the effect of initial pre-stress state leads to an increase of frequencies, in fact eRTZ results are smaller than those of Ref

[102]. Now the effect of boundary conditions and CNTs volume fraction on the fundamental frequency of sandwich

plates (L6a) with PZT-4 face-sheets and FG core (type B, Figure 4) is investigated. The results are collected in Table

23. For CCCC and SFSF, the stiffest plate is FG-X type; however, considering for SSSS and CFCF, the stiffest is FG-

Λ/FG-V and FG-$\diamond$, respectively.

Table 23. Fundamental non-dimensional circular frequencies $\omega = \frac{\omega a^2}{h} \sqrt{\frac{\rho_f}{E_{1f}}}$ for square sandwich plate (L6a) with FG-CNTRC core and PZT-4 face-sheet ($a/h{=}10$). $N_1 = N_2 = 10$

CCCC	$\overline{\omega}$				
V_{cnt}^*	**FG-U**	**FG-Λ**	**FG-V**	**FG-$\diamond$**	**FG-X**
0.11	4.0264	4.0475	4.0475	4.0117	4.0540
0.14	4.0936	4.1377	4.1377	4.0869	4.1339
0.17	4.8601	4.9384	4.9384	4.8873	4.8998
CFCF	$\overline{\omega}$				
V_{cnt}^*	**FG-U**	**FG-Λ**	**FG-V**	**FG-$\diamond$**	**FG-X**
0.11	2.8245	2.8517	2.8517	2.8153	2.8512
0.14	2.8730	2.9302	2.9302	2.8793	2.9128
0.17	3.4180	3.5164	3.5164	3.4716	3.4526
SFSF (8)	$\overline{\omega}$				
V_{cnt}^*	**FG-U**	**FG-Λ**	**FG-V**	**FG-$\diamond$**	**FG-X**
0.11	2.3573	2.3450	2.3450	2.3329	2.3660
0.14	2.4143	2.4099	2.4099	2.4034	2.4137
0.17	2.8594	2.8426	2.8426	2.8236	2.8647
SSSS (8)	$\overline{\omega}$				
V_{cnt}^*	**FG-U**	**FG-Λ**	**FG-V**	**FG-$\diamond$**	**FG-X**
0.11	3.5242	3.5279	3.5279	3.5295	3.5212
0.14	3.5808	3.5901	3.5901	3.5934	3.5756
0.17	4.1973	4.2088	4.2088	4.2139	4.1878

4 Concluding Remarks

In this work, the accuracy and reliability of the extended Refined Zigzag Theory (eRZT) are assessed for the analysis of

bending, free vibration and buckling of functionally graded carbon nanotube-reinforced (FG-CNR) sandwich plates. For

five different functionally graded topologies (FG-U, FG-V, FG-Λ, FG-$\diamond$, FG-X), the mechanical properties of face-

sheets or core layers are derived using the extended rule of mixture (eROM). Then using the D'Alembert principle the

governing equations for bending, free vibration and buckling are derived. Based on the Ritz method, a Matlab® software

has been developed. First, a preliminary comparative study of convergence characteristics of Gramm-Schmidt (GS)

orthogonal and non-orthogonal polynomials for static and dynamic analysis has been performed. The GS orthogonal

polynomials functions appear to be the most performant and are used in this work. Rectangular and square sandwich

plates with various boundary conditions and FG-CNTRC face-sheets (type A) or core (type B) have been considered.

For static case, a comparison between eRZT and other theories such as CPT, FSDT with different shear correction

factors, Reddy's TSDT and Pagano 3D exact elasticity solution are made. The numerical results show the capability of eRZT to accurately predict the bending, free vibration and buckling (under uni-axial, bi-axial compression and in-plane shear loads) behavior of sandwich plate respect other theories, especially Reddy's TSDT. Subsequently, the effect of FG topology, CNTs volume fractions and boundary conditions has been investigated. In particular, numerical results for boundary conditions other than simply supported on all edges are really scarce in the open literature. Thus, with the aim to fill this gap, new cases are analyzed with different BCs, geometry and FG topologies. From the bending results, it is concluded that increasing the CNTs volume fraction and using an FG Λ-V (for sandwich type A) or FG-X (for sandwich type B) increases the flexural stiffness and, consequently, decreases the maximum deflection; on the contrary, FG V-Λ or FG-◊ topologies have the lowest stiffness. As expected, the BCs influence the sandwich stiffness; in fact, increasing the degree of constraint on the plate edges (CCCC>CFCF>SSSS) increases the plate bending stiffness. It is interesting to note that for a cantilever rectangular sandwich plate with FG-CNTRC face-sheets under uniform pressure, the effect of CNTs reinforcement distributions for bending stiffness is very evident, this is important to aeronautical structural aims. Various BCs, FG topologies and in-plane compressive loads are taken into consideration in analyzing the buckling loads of rectangular FG-CNTRC sandwich plates. Results of buckling loads show a very strong dependence between the stiffness of these FG-CNTRC sandwich plates and the BCs, in addition to the type of compressive loads (see, Tables 14 and 15). From the numerical results, it is evident how the highest values are obtained for FG Λ-V typology sandwich and the lowest for FG V-Λ topology. Especially for in-plane shear buckling problem, the BCs and geometry of sandwich influence the buckling mode. Generally, the lowest buckling load parameters correspond to the first buckling mode, but the effect of BCs and loading type (i.e uni-axial, bi-axial compression or in-plane shear load) leads to the lowest buckling parameter for buckling modes with either two or three half-waves. Wherein possible, a comparison with sandwich plate with piezoelectric face-sheets and FG-CNTR composite core is made. The eRZT results are very close to the 3D-Finite Layer Method used for these types of plates. As expected, in this analysis neglecting the initial membrane traction stress-state for the piezoelectric face-sheets results in lowest critical buckling loads. This effect, as we said, is stronger in thin FG-CNTRC sandwich plates than thick ones. Finally, the free vibration problem has been analyzed. A comparison between present eRZT and results of other theories, coming from open literature, is made. From a comparison with the results obtained using a kinematics based on HSAPT (see, Table 19), it is concluded that eRZT is very well suited to compute the natural frequencies and the modal shapes for different types of CNTs functionally graded face-sheet sandwich plates, while retaining its simplicity. The first natural frequencies are weakly dependent on the CNTs grading laws. In these cases, the most evident effects concerning the stiffness of sandwich plates are the BCs, the grading laws and the geometry. As expected, fully clamped BCs give the highest natural frequencies. FG X-X, FG Λ-V and FG-X are preferred to others grading laws for their high flexural

36

stiffness, but in some combination of BCs, geometry and FG cases others CNTs arrangement might be considered, as for the bending case, the cantilever FG-CNTRC sandwich plate has the highest frequencies for the FG Λ-V topology. The effect of BCs and CNTs topology for a sandwich with piezoelectric face-sheets is analysed and, as for the buckling problems, it is found a strong relationship between BCs and FG topology for moderately thick plates.

In conclusion, this work shows the superior capability of eRZT to predict the global and local response for sandwich plates with different functionally graded CNTRC face-sheets (type A) or core (type B), boundary conditions and geometry. Moreover, a strong dependence among these parameters has been highlighted. It is concluded that the eRZT with Ritz method generally provides a valid tool for studying CNTRC sandwich plate. Last but not least, it should be noted that the implementation of eRZT in FEM codes requires only C^0 shape functions.

Appendix

The Ritz method-Assumed trial functions

As we said, in Ritz method the *trial* functions (also known as generalized functions) must be linearly independent and individually satisfy at least the kinematic boundary conditions, i.e., they must be a complete set of admissible functions. The choice of the admissible functions is a very important step because the convergence rate of the approximate solution depends on them. Commonly used admissible functions are polynomials, although there are examples where other types of admissible functions have been employed; for example, characteristic (modal shapes) functions of the problem of low order, i.e., modes of beam for the analysis of vibration of plates, Chebyshev polynomials and so on [32,100].

In this research, simple polynomials and Gram-Schmidt (GS) orthogonal polynomials are used as generalized Ritz functions. The GS polynomials can accommodate various kinematic boundary conditions. Moreover, in our experience they present fast convergence characteristics when compared to other polynomial admissible functions. Moreover, being orthogonal, they yield a diagonal mass matrix. Here below the procedure for constructing such polynomials is summarized.

Let $g(\xi)$ be the one-dimensional Gram-Schmidt polynomial with $\xi \in [-1,1]$; the recurrence formula is

$$g_{m+1}(\xi) \equiv (\xi - A_m) g_m(\xi) - B_m g_{m-1}(\xi) \qquad (m=1,2,\ldots) \qquad (A.1)$$

with

$$A_m \equiv \frac{\int_{-1}^{+1} \xi g_{m+1}^2(\xi) d\xi}{\int_{-1}^{+1} g_m^2(\xi) d\xi}, \quad B_m \equiv \frac{\int_{-1}^{+1} g_m^2(\xi) d\xi}{\int_{-1}^{+1} g_{m-1}^2(\xi) d\xi} \qquad (A.2)$$

and

$$g_0(\xi) = 0; \qquad g_1(\xi) = b_1(\xi)^{\Omega_1} b_2(\xi)^{\Omega_2} \tag{A.3}$$

where in general

$$b_i(\xi) = 0 \tag{A.4}$$

is the equation of the edge ith. For the one-dimensional problem at the hand,

$$b_1(\xi) = 1 + \xi \quad \text{and} \quad b_2(\xi) = 1 - \xi. \tag{A.5}$$

In Eq. (A.3) the values of the exponents depend on the boundary conditions: 0 if the function does not vanish, 1 if the function vanishes (for the problem at hand, see Table A.2).

As usual, the two-dimensional admissible functions are written as a product of one-dimensional Gram-Schmidt polynomials. Thus, for the general unknown function (43), we write

$$\hat{f}(\xi_1, \xi_2, t) = \sum_{p=1}^{P(f)} \sum_{r=1}^{R(f)} C_{pr}^{(f)}(t) g_p^{(f)}(\xi_1) g_r^{(f)}(\xi_2) = \sum_{m=1}^{M(f)} C_m^{(f)}(t) g_m^{(f)}(\xi_1, \xi_2) \tag{A.6}$$

with

$$m = (p-1)R(f) + r \tag{A.7}$$

The first basis function is given by

$$g_1^{(f)}(\xi_1, \xi_2) = \prod_{j=1}^{n_l} \left[\chi_j(\xi_1, \xi_2) \right]^{\Omega_j^{(f)}} \tag{A.8}$$

where n_l gives the number of the plate edges (for qua adrilateral plate, $n_l = 4$), $\chi_j(\xi_1, \xi_2) = 0$ is the equations of the jth edge of the plate, the exponents Ω_j are chosen such that the geometric (prescribed) boundary condition on the edge for the function $\hat{f}(\xi_1, \xi_2, t)$ be satisfied.

For example, for the plate shown in fig. 1, the functions $\chi_j(\xi_1, \xi_2)$ are:

$$\chi_1(\xi_1, \xi_2) = (\xi_1 + 1), \; \chi_2(\xi_1, \xi_2) = (\xi_2 + 1), \; \chi_3(\xi_1, \xi_2) = (\xi_1 - 1), \; \chi_4(\xi_1, \xi_2) = (\xi_2 - 1)$$

Tables A.1 and A.2 give the prescribed (geometric) boundary conditions of eRZT (see, Ref. [88]) and the corresponding exponents $\Omega_j^{(f)}$, respectively.

Table A.1- Prescribed (geometric) boundary conditions of eRZT.

Edge F	$u_\alpha,\ w,\ \theta_\alpha,\ \psi_\alpha$ free
Edge $\xi_1 = \mp 1$ SS	$u_1 = w = \theta_1 = \psi_1 = 0;\ u_2,\ \theta_2,\ \psi_2$ free
Edge $\xi_2 = \mp 1$ SS	$u_2 = w = \theta_2 = \psi_2 = 0;\ u_1,\ \theta_1,\ \psi_1$ free
Edge C	$u_\alpha = w = \theta_\alpha = \psi_\alpha = 0$
F=free, C= clamped, SS=simply supported	

Table A.2 – Exponents for the classical geometric boundary conditions.

edge $\xi_1 = \mp 1$ SS	$\Omega_j^{u_1} = \Omega_j^{\theta_1} = \Omega_j^{\psi_1} = 0$ $\Omega_j^{u_2} = \Omega_j^{\theta_2} = \Omega_j^{\psi_2} = 1$
edge $\xi_2 = \mp 1$ SS	$\Omega_j^{u_1} = \Omega_j^{\theta_1} = \Omega_j^{\psi_1} = 1$ $\Omega_j^{u_2} = \Omega_j^{\theta_2} = \Omega_j^{\psi_2} = 0$
edge SS	$\Omega_j^{w} = 1$
edge F	$\Omega_j^{f} = 0$
edge C	$\Omega_j^{f} = 1$

REFERENCES

[1]   Birman V, Kardomateas GA. Review of current trends in research and applications of sandwich structures. Composites Part B: Engineering 2018;142:221–40. doi:10.1016/j.compositesb.2018.01.027.

[2]   Rayjade GR. Study of Composite Sandwich Structure and Bending Characteristics– A Review. International Journal of Current Engineering and Technology 2015;5:6.

[3]   Takeda N, Minakuchi S, Okabe Y. Smart Composite Sandwich Structures for Future Aerospace Application - Damage Detection and Suppression-: a Review. Journal of Solid Mechanics and Materials Engineering 2007;1:3–17. doi:10.1299/jmmp.1.3.

[4]   Koizumi M, Niino M. Overview of FGM Research in Japan. MRS Bulletin 1995;20:19–21. doi:10.1557/S0883769400048867.

[5]   Sayyad AS, Ghugal YM. Effects of nonlinear hygrothermomechanical loading on bending of FGM rectangular plates resting on two-parameter elastic foundation using four-unknown plate theory. Journal of Thermal Stresses 2018:1–20. doi:10.1080/01495739.2018.1469962.

[6]   Koizumi M. FGM activities in Japan. Composites Part B: Engineering 1997;28:1–4. doi:10.1016/S1359-8368(96)00016-9.

[7]   Müller E, Drašar Č, Schilz J, Kaysser WA. Functionally graded materials for sensor and energy applications. Materials Science and Engineering: A 2003;362:17–39. doi:10.1016/S0921-5093(03)00581-1.

[8]   Pompe W, Worch H, Epple M, Friess W, Gelinsky M, Greil P, et al. Functionally graded materials for biomedical applications. Materials Science and Engineering: A 2003;362:40–60. doi:10.1016/S0921-5093(03)00580-X.

[9]   Schulz U, Peters M, Bach Fr-W, Tegeder G. Graded coatings for thermal, wear and corrosion barriers. Materials Science and Engineering: A 2003;362:61–80. doi:10.1016/S0921-5093(03)00579-3.

[10]   Mahamood RM, Akinlabi ET, Shukla M, Pityana S. Functionally Graded Material: An Overview. Proceedings of the World Congress on Engineering 2012;III:5.

[11] Tarlochan F. Functionally Graded Material: A New Breed of Engineered Material. Journal of Applied Mechanical Engineering 2012;1:2. doi:10.4172/2168-9873.1000e115.

[12] Ferreira AJM, Batra RC, Roque CMC, Qian LF, Martins PALS. Static analysis of functionally graded plates using third-order shear deformation theory and a meshless method. Composite Structures 2005;69:449–57. doi:10.1016/j.compstruct.2004.08.003.

[13] Ferreira AJM, Roque CMC, Jorge RMN, Fasshauer GE, Batra RC. Analysis of Functionally Graded Plates by a Robust Meshless Method. Mechanics of Advanced Materials and Structures 2007;14:577–87. doi:10.1080/15376490701672732.

[14] Ferreira AJM, Batra RC, Roque CMC, Qian LF, Jorge RMN. Natural frequencies of functionally graded plates by a meshless method. Composite Structures 2006;75:593–600. doi:10.1016/j.compstruct.2006.04.018.

[15] Sun CH, Li F, Cheng HM, Lu GQ. Axial Young's modulus prediction of single-walled carbon nanotube arrays with diameters from nanometer to meter scales. Applied Physics Letters 2005;87:3. doi:10.1063/1.2119409.

[16] Jia J, Zhao J, Xu G, Di J, Yong Z, Tao Y, et al. A comparison of the mechanical properties of fibers spun from different carbon nanotubes. Carbon 2011;49:1333–9. doi:10.1016/j.carbon.2010.11.054.

[17] Thostenson ET, Chou T-W. Aligned multi-walled carbon nanotube-reinforced composites: processing and mechanical characterization. Journal of Physics D: Applied Physics 2002;35:L77–80. doi:10.1088/0022-3727/35/16/103.

[18] Hedayati H, Sobhani Aragh B. Influence of graded agglomerated CNTs on vibration of CNT-reinforced annular sectorial plates resting on Pasternak foundation. Applied Mathematics and Computation 2012;218:8715–35. doi:10.1016/j.amc.2012.01.080.

[19] Tagrara SH, Benachour A, Bouiadjra MB, Tounsi A. On bending, buckling and vibration responses of functionally graded carbon nanotube-reinforced composite beams. Steel and Composite Structures 2015;19:1259–77. doi:10.12989/scs.2015.19.5.1259.

[20] Chaht FL, Kaci A, Houari MSA, Tounsi A, Beg OA, Mahmoud SR. Bending and buckling analyses of functionally graded material (FGM) size-dependent nanoscale beams including the thickness stretching effect. Steel and Composite Structures 2015;18:425–42. doi:10.12989/scs.2015.18.2.425.

[21] Thai CH, Ferreira AJM, Rabczuk T, Nguyen-Xuan H. Size-dependent analysis of FG-CNTRC microplates based on modified strain gradient elasticity theory. European Journal of Mechanics - A/Solids 2018;72:521–38. doi:10.1016/j.euromechsol.2018.07.012.

[22] Loos M. Applications of CNTs. Carbon Nanotube Reinforced Composites, Elsevier; 2015, p. 189–205. doi:10.1016/B978-1-4557-3195-4.00007-2.

[23] Gibson RF, Ayorinde EO, Wen Y-F. Vibrations of carbon nanotubes and their composites: A review. Composites Science and Technology 2007;67:1–28. doi:10.1016/j.compscitech.2006.03.031.

[24] Formica G, Lacarbonara W, Alessi R. Vibrations of carbon nanotube-reinforced composites. Journal of Sound and Vibration 2010;329:1875–89. doi:10.1016/j.jsv.2009.11.020.

[25] Shen H-S. Nonlinear bending of functionally graded carbon nanotube-reinforced composite plates in thermal environments. Composite Structures 2009;91:9–19. doi:10.1016/j.compstruct.2009.04.026.

[26] Shen H-S, Zhang C-L. Thermal buckling and postbuckling behavior of functionally graded carbon nanotube-reinforced composite plates. Materials & Design 2010;31:3403–11. doi:10.1016/j.matdes.2010.01.048.

[27] Wang Z-X, Shen H-S. Nonlinear vibration of nanotube-reinforced composite plates in thermal environments. Computational Materials Science 2011;50:2319–30. doi:10.1016/j.commatsci.2011.03.005.

[28] Wang Z-X, Shen H-S. Nonlinear vibration and bending of sandwich plates with nanotube-reinforced composite face sheets. Composites Part B: Engineering 2012;43:411–21. doi:10.1016/j.compositesb.2011.04.040.

[29] Kaci A, Tounsi A, Bakhti K, Adda Bedia EA. Nonlinear cylindrical bending of functionally graded carbon nanotube-reinforced composite plates. Steel and Composite Structures 2012;12:491–504. doi:10.12989/scs.2012.12.6.491.

[30] Liew KM, Lei ZX, Zhang LW. Mechanical analysis of functionally graded carbon nanotube reinforced composites: A review. Composite Structures 2015;120:90–7. doi:10.1016/j.compstruct.2014.09.041.

[31] Alibeigloo A, Liew KM. Thermoelastic analysis of functionally graded carbon nanotube-reinforced composite plate using theory of elasticity. Composite Structures 2013;106:873–81. doi:10.1016/j.compstruct.2013.07.002.

[32] Kumar P, Srinivas J. Vibration, buckling and bending behavior of functionally graded multi-walled carbon nanotube reinforced polymer composite plates using the layer-wise formulation. Composite Structures 2017;177:158–70. doi:10.1016/j.compstruct.2017.06.055.

[33] Phung-Van P, Abdel-Wahab M, Liew KM, Bordas SPA, Nguyen-Xuan H. Isogeometric analysis of functionally graded carbon nanotube-reinforced composite plates using higher-order shear deformation theory. Composite Structures 2015;123:137–49. doi:10.1016/j.compstruct.2014.12.021.

[34] Jafari Mehrabadi S, Sobhani Aragh B, Khoshkhahesh V, Taherpour A. Mechanical buckling of nanocomposite rectangular plate reinforced by aligned and straight single-walled carbon nanotubes. Composites Part B: Engineering 2012;43:2031–40. doi:10.1016/j.compositesb.2012.01.067.

[35] Zhang LW, Lei ZX, Liew KM. Computation of vibration solution for functionally graded carbon nanotube-reinforced composite thick plates resting on elastic foundations using the element-free IMLS-Ritz method. Applied Mathematics and Computation 2015;256:488–504. doi:10.1016/j.amc.2015.01.066.

[36] Vo-Duy T, Ho-Huu V, Nguyen-Thoi T. Free vibration analysis of laminated FG-CNT reinforced composite beams using finite element method. Front Struct Civ Eng 2018;13:324–36. doi:10.1007/s11709-018-0466-6.

[37] Wang A, Chen H, Hao Y, Zhang W. Vibration and bending behavior of functionally graded nanocomposite doubly-curved shallow shells reinforced by graphene nanoplatelets. Results in Physics 2018;9:550–9. doi:10.1016/j.rinp.2018.02.062.

[38] Srivastava A, Kumar D. Post-buckling behaviour of carbon-nanotube-reinforced nanocomposite plate. Sādhanā 2017;42:129–41. doi:10.1007/s12046-016-0581-9.

[39] Song M, Kitipornchai S, Yang J. Free and forced vibrations of functionally graded polymer composite plates reinforced with graphene nanoplatelets. Composite Structures 2017;159:579–88. doi:10.1016/j.compstruct.2016.09.070.

[40] Song M, Yang J, Kitipornchai S, Zhu W. Buckling and postbuckling of biaxially compressed functionally graded multilayer graphene nanoplatelet-reinforced polymer composite plates. International Journal of Mechanical Sciences 2017;131–132:345–55. doi:10.1016/j.ijmecsci.2017.07.017.

[41] Kiani Y. Thermal post-buckling of FG-CNT reinforced composite plates. Composite Structures 2017;159:299–306. doi:10.1016/j.compstruct.2016.09.084.

[42] Lei ZX, Zhang LW, Liew KM. Elastodynamic analysis of carbon nanotube-reinforced functionally graded plates. International Journal of Mechanical Sciences 2015;99:208–17. doi:10.1016/j.ijmecsci.2015.05.014.

[43] Sankar A, Natarajan S, Ganapathi M. Dynamic instability analysis of sandwich plates with CNT reinforced facesheets. Composite Structures 2016;146:187–200. doi:10.1016/j.compstruct.2016.03.026.

[44] Jam JE, Kiani Y. Low velocity impact response of functionally graded carbon nanotube reinforced composite beams in thermal environment. Composite Structures 2015;132:35–43. doi:10.1016/j.compstruct.2015.04.045.

[45] Yang C-H, Ma W-N, Ma D-W, He Q, Zhong J-L. Analysis of the low velocity impact response of functionally graded carbon nanotubes reinforced composite spherical shells. J Mech Sci Technol 2018;32:2681–91. doi:10.1007/s12206-018-0525-x.

[46] Lin F, Xiang Y. Vibration of carbon nanotube reinforced composite beams based on the first and third order beam theories. Applied Mathematical Modelling 2014;38:3741–54. doi:10.1016/j.apm.2014.02.008.

[47] Reddy JN. Mechanics of Laminated Composite Plates and Shells : Theory and Analysis, Second Edition. CRC Press; 2003. doi:10.1201/b12409.

[48] Jalali SK, Heshmati M. Buckling analysis of circular sandwich plates with tapered cores and functionally graded carbon nanotubes-reinforced composite face sheets. Thin-Walled Structures 2016;100:14–24. doi:10.1016/j.tws.2015.12.001.

[49] Wattanasakulpong N, Chaikittiratana A. Exact solutions for static and dynamic analyses of carbon nanotube-reinforced composite plates with Pasternak elastic foundation. Applied Mathematical Modelling 2015;39:5459–72. doi:10.1016/j.apm.2014.12.058.

[50] Zhang LW. Geometrically nonlinear large deformation of CNT-reinforced composite plates with internal column supports. Journal of Modeling in Mechanics and Materials 2017;1:22. doi:10.1515/jmmm-2016-0154.

[51] Natarajan S, Haboussi M, Manickam G. Application of higher-order structural theory to bending and free vibration analysis of sandwich plates with CNT reinforced composite facesheets. Composite Structures 2014;113:197–207. doi:10.1016/j.compstruct.2014.03.007.

[52] Natarajan S, Ganapathi M. Bending and vibration of functionally graded material sandwich plates using an accurate theory. Finite Elements in Analysis and Design 2012;57:32–42. doi:10.1016/j.finel.2012.03.006.

[53] Sankar A, Natarajan S, Merzouki T, Ganapathi M. Nonlinear Dynamic Thermal Buckling of Sandwich Spherical and Conical Shells with CNT Reinforced Facesheets. International Journal of Structural Stability and Dynamics 2017;17:1750100. doi:10.1142/S0219455417501000.

[54] George N, Jeyaraj P, Murigendrappa SM. Buckling and Free Vibration of Nonuniformly Heated Functionally Graded Carbon Nanotube Reinforced Polymer Composite Plate. Int J Str Stab Dyn 2016;17:1750064. doi:10.1142/S021945541750064X.

[55] Chavan SG, Lal A. Bending analysis of laminated SWCNT Reinforced functionally graded plate Using FEM. Curved and Layered Structures 2017;4. doi:10.1515/cls-2017-0010.

[56] Ansari M, Kumar A, Fic S, Barnat-Hunek D. Flexural and Free Vibration Analysis of CNT-Reinforced Functionally Graded Plate. Materials 2018;11:2387. doi:10.3390/ma11122387.

[57] Nguyen Dinh D, Nguyen PD. The Dynamic Response and Vibration of Functionally Graded Carbon Nanotube-Reinforced Composite (FG-CNTRC) Truncated Conical Shells Resting on Elastic Foundations. Materials (Basel) 2017;10. doi:10.3390/ma10101194.

[58] Moradi-Dastjerdi R, Momeni-Khabisi H. Vibrational behavior of sandwich plates with functionally graded wavy carbon nanotube-reinforced face sheets resting on Pasternak elastic foundation. Journal of Vibration and Control 2018;24:2327–43. doi:10.1177/1077546316686227.

[59] Huang Y, Yang Z, Liu A, Fu J. Nonlinear Buckling Analysis of Functionally Graded Graphene Reinforced Composite Shallow Arches with Elastic Rotational Constraints under Uniform Radial Load. Materials (Basel) 2018;11. doi:10.3390/ma11060910.

[60] Rout M, Dash C, Karmakar A. Low velocity impact performance of CNTs-reinforced composite plate. International Journal of Advanced Mechanical Engineering 2018;8:8.

[61] Mehar K, Panda SK, Dehengia A, Kar VR. Vibration analysis of functionally graded carbon nanotube reinforced composite plate in thermal environment. Journal of Sandwich Structures & Materials 2016;18:151–73. doi:10.1177/1099636215613324.

[62] Zhang LW. An element-free based IMLS-Ritz method for buckling analysis of nanocomposite plates of polygonal planform. Engineering Analysis with Boundary Elements 2017;77:10–25. doi:10.1016/j.enganbound.2017.01.004.

[63]   Zhang LW, Lei ZX, Liew KM. Vibration characteristic of moderately thick functionally graded carbon nanotube reinforced composite skew plates. Composite Structures 2015;122:172–83. doi:10.1016/j.compstruct.2014.11.070.

[64]   Kiani Y. Free vibration of FG-CNT reinforced composite skew plates. Aerospace Science and Technology 2016;58:178–88. doi:10.1016/j.ast.2016.08.018.

[65]   Zhang LW, Xiao LN, Zou GL, Liew KM. Elastodynamic analysis of quadrilateral CNT-reinforced functionally graded composite plates using FSDT element-free method. Composite Structures 2016;148:144–54. doi:10.1016/j.compstruct.2016.04.006.

[66]   Ansari R, Torabi J, Shojaei MF. Buckling and vibration analysis of embedded functionally graded carbon nanotube-reinforced composite annular sector plates under thermal loading. Composites Part B: Engineering 2017;109:197–213. doi:10.1016/j.compositesb.2016.10.050.

[67]   Ansari R, Torabi J, Hosein Shakouri A. Vibration analysis of functionally graded carbon nanotube-reinforced composite elliptical plates using a numerical strategy. Aerospace Science and Technology 2017;60:152–61. doi:10.1016/j.ast.2016.11.004.

[68]   Lei ZX, Liew KM, Yu JL. Free vibration analysis of functionally graded carbon nanotube-reinforced composite plates using the element-free kp-Ritz method in thermal environment. Composite Structures 2013;106:128–38. doi:10.1016/j.compstruct.2013.06.003.

[69]   Mirzaei M, Kiani Y. Nonlinear free vibration of temperature-dependent sandwich beams with carbon nanotube-reinforced face sheets. Acta Mechanica 2016;227:1869–84. doi:10.1007/s00707-016-1593-6.

[70]   Bhardwaj G, Upadhyay AK, Pandey R, Shukla KK. Non-linear flexural and dynamic response of CNT reinforced laminated composite plates. Composites Part B: Engineering 2013;45:89–100. doi:10.1016/j.compositesb.2012.09.004.

[71]   Selim BA, Zhang LW, Liew KM. Vibration analysis of CNT reinforced functionally graded composite plates in a thermal environment based on Reddy's higher-order shear deformation theory. Composite Structures 2016;156:276–90. doi:10.1016/j.compstruct.2015.10.026.

[72]   Mehar K, Panda SK. Geometrical nonlinear free vibration analysis of FG-CNT reinforced composite flat panel under uniform thermal field. Composite Structures 2016;143:336–46. doi:10.1016/j.compstruct.2016.02.038.

[73]   Lei ZX, Liew KM, Yu JL. Buckling analysis of functionally graded carbon nanotube-reinforced composite plates using the element-free kp-Ritz method. Composite Structures 2013;98:160–8. doi:10.1016/j.compstruct.2012.11.006.

[74]   Lei ZX, Zhang LW, Liew KM. Buckling analysis of CNT reinforced functionally graded laminated composite plates. Composite Structures 2016;152:62–73. doi:10.1016/j.compstruct.2016.05.047.

[75]   Phung-Van P, Luong-Van H, Nguyen-Thoi T, Nguyen-Xuan H. A cell-based smoothed discrete shear gap method (CS-FEM-DSG3) based on the C0-type higher-order shear deformation theory for dynamic responses of Mindlin plates on viscoelastic foundations subjected to a moving sprung vehicle. International Journal for Numerical Methods in Engineering 2014;98:988–1014. doi:10.1002/nme.4662.

[76]   Phung-Van P, Nguyen-Thoi T, Luong-Van H, Thai-Hoang C, Nguyen-Xuan H. A cell-based smoothed discrete shear gap method (CS-FEM-DSG3) using layerwise deformation theory for dynamic response of composite plates resting on viscoelastic foundation. Computer Methods in Applied Mechanics and Engineering 2014;272:138–59. doi:10.1016/j.cma.2014.01.009.

[77]   Phung-Van P, Thai CH, Nguyen-Thoi T, Nguyen-Xuan H. Static and free vibration analyses of composite and sandwich plates by an edge-based smoothed discrete shear gap method (ES-DSG3) using triangular elements based on layerwise theory. Composites Part B: Engineering 2014;60:227–38. doi:10.1016/j.compositesb.2013.12.044.

[78]   Phung-Van P, Nguyen-Thoi T, Luong-Van H, Lieu-Xuan Q. Geometrically nonlinear analysis of functionally graded plates using a cell-based smoothed three-node plate element (CS-MIN3) based on the C0-HSDT. Computer Methods in Applied Mechanics and Engineering 2014;270:15–36. doi:10.1016/j.cma.2013.11.019.

[79]   Phung-Van P, Nguyen-Thoi T, Bui-Xuan T, Lieu-Xuan Q. A cell-based smoothed three-node Mindlin plate element (CS-FEM-MIN3) based on the C0-type higher-order shear deformation for geometrically nonlinear analysis of laminated composite plates. Computational Materials Science 2015;96:549–58. doi:10.1016/j.commatsci.2014.04.043.

[80]   Wu C-P, Chang S-K. Stability of carbon nanotube-reinforced composite plates with surface-bonded piezoelectric layers and under bi-axial compression. Composite Structures 2014;111:587–601. doi:10.1016/j.compstruct.2014.01.040.

[81]   Kolahchi R, Zarei MS, Hajmohammad MH, Nouri A. Wave propagation of embedded viscoelastic FG-CNT-reinforced sandwich plates integrated with sensor and actuator based on refined zigzag theory. International Journal of Mechanical Sciences 2017;130:534–45. doi:10.1016/j.ijmecsci.2017.06.039.

[82]   Ghorbanpour Arani A, Mosayyebi M, Kolahdouzan F, Kolahchi R, Jamali M. Refined zigzag theory for vibration analysis of viscoelastic functionally graded carbon nanotube reinforced composite microplates integrated with piezoelectric layers. Proceedings of the Institution of Mechanical Engineers, Part G: Journal of Aerospace Engineering 2017;231:2464–78. doi:10.1177/0954410016667150.

[83]   Hajmohammad MH, Nouri AH, Zarei MS, Kolahchi R. A new numerical approach and visco-refined zigzag theory for blast analysis of auxetic honeycomb plates integrated by multiphase nanocomposite facesheets in hygrothermal environment. Engineering with Computers 2018:17. doi:10.1007/s00366-018-0655-x.

[84]   Tessler A, Di Sciuva M, Gherlone M. Refinement of Timoshenko Beam Theory for Composite and Sandwich Beams using Zigzag Kinematics. NASA/TP-2007-215086 2007:1–45.

[85]   Tessler A, Di Sciuva M, Gherlone M. A Refined Zigzag Beam Theory for Composite and Sandwich Beams. Journal of Composite Materials 2009;43:1051–81. doi:10.1177/0021998308097730.

[86]   Di Sciuva M, Gherlone M, Tessler A. A Robust and Consistent First-Order Zigzag Theory for Multilayered Beams. In: Gilat R, Banks-Sills L, editors. Advances in Mathematical Modeling and Experimental Methods for Materials and Structures: The Jacob Aboudi Volume, Dordrecht: Springer Netherlands; 2009, p. 255–68. doi:10.1007/978-90-481-3467-0_20.

[87]   Tessler A, Di Sciuva M, Gherlone M. A consistent refinement of first-order shear-deformation theory for laminated composite and sandwich plates using improved zigzag kinematics 2010;5:341–67. doi:10.2140/jomms.2010.5.341.

[88]   Tessler A, Sciuva MD, Gherlone M. Refined Zigzag Theory for Laminated Composite and Sandwich Plates. NASA/TP-2009-215561 2009:1–53.

[89]   Versino D. Refined theories and Discontinuous Galerkin methods for the analysis of multilayered composite structures. PhD Thesis. Politecnico di Torino, 2012.

[90]   Iurlaro L, Gherlone M, Di Sciuva M, Tessler A. Assessment of the Refined Zigzag Theory for bending, vibration, and buckling of sandwich plates: a comparative study of different theories. Composite Structures 2013;106:777–92. doi:10.1016/j.compstruct.2013.07.019.

[91]   Iurlaro L, Gherlone M, Di Sciuva M, Tessler A. A Multi-scale Refined Zigzag Theory for Multilayered Composite and Sandwich Plates with Improved Transverse Shear Stresses, Ibiza, Spain: 2013.

[92]   Iurlaro L, Gherlone M, Di Sciuva M. A comparison of zigzag functions for the bending, vibration and buckling analysis of multilayered composite and sandwich plates. XI World Congress on Computational Mechanics, Barcelona, Spain 2014:13.

[93]   Iurlaro L, Gherlone M, Di Sciuva M. Bending and free vibration analysis of functionally graded sandwich plates using the Refined Zigzag Theory. Jnl of Sandwich Structures & Materials 2014;16:669–99. doi:10.1177/1099636214548618.

[94]   Gherlone M, Tessler A, Di Sciuva M. C0 beam elements based on the Refined Zigzag Theory for multilayered composite and sandwich laminates. Composite Structures 2011;93:2882–94. doi:10.1016/j.compstruct.2011.05.015.

[95]   Iurlaro L. Development of refined models for multilayered composite and sandwich structures: analytical formulation, FEM implementation and experimental assessment. PhD Thesis. Politecnico di Torino, 2015.

[96]   Di Sciuva M, Gherlone M, Iurlaro L, Tessler A. A class of higher-order C0 composite and sandwich beam elements based on the Refined Zigzag Theory. Composite Structures 2015;132:784–803. doi:10.1016/j.compstruct.2015.06.071.

[97]   Di Sciuva M, Sorrenti M. Bending and free vibration analysis of functionally graded sandwich plates: An assessment of the Refined Zigzag Theory. Journal of Sandwich Structures & Materials 2019:1–43. doi:10.1177/1099636219843970.

[98]   García-Macías E, Guzmán CF, Saavedra Flores EI, Castro-Triguero R. Multiscale modeling of the elastic moduli of CNT-reinforced polymers and fitting of efficiency parameters for the use of the extended rule-of-mixtures. Composites Part B: Engineering 2019;159:114–31. doi:10.1016/j.compositesb.2018.09.057.

[99]   Birman V, Byrd LW. Modeling and Analysis of Functionally Graded Materials and Structures. Appl Mech Rev 2007;60:195–216. doi:10.1115/1.2777164.

[100] Moreno-García P, dos Santos JVA, Lopes H. A Review and Study on Ritz Method Admissible Functions with Emphasis on Buckling and Free Vibration of Isotropic and Anisotropic Beams and Plates. Archives of Computational Methods in Engineering 2018;25:785–815. doi:10.1007/s11831-017-9214-7.

[101] Mohammadimehr M, Mostafavifar M. Free vibration analysis of sandwich plate with a transversely flexible core and FG-CNTs reinforced nanocomposite face sheets subjected to magnetic field and temperature-dependent material properties using SGT. Composites Part B: Engineering 2016;94:253–70. doi:10.1016/j.compositesb.2016.03.030.

[102] Wu C-P, Li W-C. Quasi-3D Stability and Vibration Analyses of Sandwich Piezoelectric Plates with an Embedded CNT-Reinforced Composite Core. International Journal of Structural Stability and Dynamics 2016;16:1450097. doi:10.1142/S0219455414500977.

[103] Pagano NJ. Exact Solutions for Rectangular Bidirectional Composites and Sandwich Plates. Journal of Composite Materials 1970;4:20–34. doi:10.1177/002199837000400102.

[104] Shen H-S, Zhu ZH. Postbuckling of sandwich plates with nanotube-reinforced composite face sheets resting on elastic foundations. European Journal of Mechanics - A/Solids 2012;35:10–21. doi:10.1016/j.euromechsol.2012.01.005.

[105] Madabhusi-Raman P, Davalos JF. Static shear correction factor for laminated rectangular beams. Composites Part B: Engineering 1996;27:285–93. doi:10.1016/1359-8368(95)00014-3.

[106] Yang M, Qiao P. Higher-order impact modeling of sandwich structures with flexible core. International Journal of Solids and Structures 2005;42:5460–90. doi:10.1016/j.ijsolstr.2005.02.037.

[107] Frostig Y, Thomsen OT. High-order free vibration of sandwich panels with a flexible core. International Journal of Solids and Structures 2004;41:1697–724. doi:10.1016/j.ijsolstr.2003.09.051.

[108] Wu Z, Chen W. High-Order Theory, Laminated Plate Buckling. In: Hetnarski RB, editor. Encyclopedia of Thermal Stresses, Springer Science; 2014, p. 2267–74.